



Study of engineering developing decagonal-like rational approximant structure of Al–Ni–Cu–Fe–Mn–Cr senary system in aluminum alloy through additive manufacturing

Kai-Chieh Chang, Fei-Yi Hung*, Jun-Ren Zhao

Department of Materials Science and Engineering, National Cheng Kung University, Tainan, 701, Taiwan



ARTICLE INFO

Keywords:

Additive manufacturing (AM)
Laser powder bed fusion (LPBF)
Aluminum alloy
Al–Ni–Cu alloy
Decagonal Quasicrystal
Rational approximant phase
STEM-HAADF

ABSTRACT

Quasi-periodic materials hold unique properties, but mass-producing bulk materials with such structures remains challenging. The rational approximant phase belongs to the Bravais crystal system but exhibits irrational cut features and diffraction symmetries, which are similar to quasicrystals. This study uses additive manufacturing (AM) and prolonged annealing to create an aluminum-based alloy featuring a quasicrystal-like rational approximant phase, $\text{Al}_6(\text{Cu, Ni})_1(\text{Cr, Mn, Fe})_1$, overcoming the production limitations of reproducible quasi-periodic materials. This phase transformation occurs at the Al–Al₉FeNi interface, resulting in a monoclinic periodic structure with long-range translational symmetry. The structure comprises sublattices of stars and compressed hexagons, forming tile mode coverings with pseudo-five-fold decagonal shield-like tiles (SLTs) through transition-element atoms. Furthermore, HAADF imaging reveals clear dark monoclinic rhombic patterns with long-range ordered translational symmetry, free from atomic defects. The rational approximant phase has been verified crystallography through X-ray diffraction, confirming its translational symmetry. Additionally, the Al₃(Zr, Sc) phase facilitates the phase transformation process through lattice interactions. These findings introduce a novel perspective on the phase transformation in decagonal-like rational approximants and broaden the realm for future engineering applications.

1. Introduction

Quasicrystals are defined by their orderly, non-periodic atomic arrangements that span two or three dimensions, featuring rotational symmetries, which are not permitted in conventional crystallography. Characterized by long-range ordered, aperiodic structures, they are distinct from regular crystals due to their lack of translational symmetries [1–4]. In metallic quasicrystals, icosahedral quasicrystals (IQC) and decagonal quasicrystals (DQC) are the most frequent systems. DQCs have been identified in multiple aluminum alloy systems [5–8]. This structure exhibits quasiperiodic properties in two dimensions while maintaining periodicity in the third dimension. Decagonal columnar clusters are commonly used to describe the building units of DQCs, and the Gummelt and Lück decagonal array modes are frequently employed to describe the stacking rule of DQC quasi-cells [9–13]. Existing literature suggests that the DQC systems' inequivalent atomic configurations in similar sublattices, characterized by their inherent irrational segmentation, exhibit metastability commonly, especially in aluminum

alloys [14–17]. This potentially poses limitations for specific applications. This study proposes a rational approximant structure with atomic arrangements that resemble those found in DQCs, featuring a similar Gummelt tiling model. However, unlike DQCs, this approximant is a fundamental part of a Bravais lattice system, marked by its periodic lattice structure and translational symmetries—attributes absent in quasicrystals [18]. This basic difference potentially endows the structure with enhanced stability [19], offering new insights into the transition from quasi-crystalline to crystalline materials.

Quasicrystals, predominantly found in binary and ternary alloy systems [20–23], are less frequently observed in more complex quaternary and quinary systems [24,25]. In general, even in multi-element quasicrystals, a limited number of elements dominate the structural composition. Building upon this understanding, this study presents an advancement: discovering a rational approximant structure composed of a senary element system. This six-element structure not only expands the scope of known rational quasicrystal-like approximants but suggests potential advantages in terms of enhancing material properties.

* Corresponding author.

E-mail address: fyhung@mail.ncku.edu.tw (F.-Y. Hung).

Producing more complex quasicrystal-like structures through conventional methods, such as arc-casting metallurgy with heat treatment, can be challenging due to differences in melting points and chemical properties. These challenges impact their practical application and scalability. Quasicrystals are renowned for their unique properties, including high hardness and wear resistance, low thermal and electrical conductivity, high mechanical strength, distinctive optical characteristics, low friction, and hydrogen storage capability [25–30]. However, stable mass production of these bulk materials has faced difficulties [31,32]. Therefore, rational approximant structures, the focus of this study, may offer a promising alternative. While retaining structures similar to quasicrystals, rational approximants provide a more stable and uniform sub-lattice arrangement, which could facilitate mass production and expand the potential applications of these materials. However, research on successfully producing a singular rational approximant phase in materials is relatively limited, and more studies are necessary to verify the applicational stability of these materials. Leveraging the high-speed solidification process inherent in laser powder bed fusion (LPBF) additive manufacturing (AM) technology offers a promising, rapid, and reproducible manufacturing solution for mass production of materials with quasicrystal-like structures. Recent literature has also begun to highlight the potential of AM for producing reproducible quasicrystal structures in bulk materials [33–35]. The literature notes that quasicrystals offer enhanced hardness and high-temperature stability as precipitation-strengthening phases in AM technology Al alloys, effectively improving the material's mechanical strength and wear resistance at elevated temperatures [36–39]. Additionally, AM allows for the customization of complex geometrical structures and saves on the costs associated with mold development. Aluminum alloys, renowned for their lightweight properties and excellent corrosion resistance, are extensively utilized across various engineering applications. Furthermore, aluminum powders are particularly advantageous in the LPBF process due to their high reflectivity and excellent thermal conductivity. These properties are crucial for enhancing formability and controlling printing defects, making AM aluminum alloys well-suited for high-performance engineering applications. The introduction of AM in quasicrystal structures, contributed by the rapid cooling rates and fine solidified texture, substantially augments these alloys' mechanical properties, corrosion resistance, and high-temperature stability. Moreover, the rapid solidification in AM enables the fusion of elements with varying properties, including melting points and chemistries, to form oversaturated solid solutions within aluminum alloys, and this process aids in forming multi-element rational approximants. Therefore, the aluminum matrix is enriched with specific elements for applications demanding lightweight, high strength, and corrosion resistance. Ni, Cu, Fe, Cr, and Mn are incorporated to create the rational approximant phase through laser powder bed fusion. Zr and Sc are also introduced to print fine-grained bulk materials [40–43]. The literature indicates that materials based on the printed Al-Ni-Cu system exhibit promising strength at both room and elevated temperatures, as well as thermal stability of the phases, which aids in the development of materials suitable for engineering applications.

In this study, the transformation process within a supersaturated senary-element solution in Al_9FeNi [44], facilitated by prolonged annealing at 580 °C for 24 h, leads to the development of a novel senary rational approximant phase with cluster types similar to those in DQCs. It is a noteworthy contribution to the field, considering the relatively less research on DQC approximants than IQCs [45,46]. Furthermore, this research emphasizes investigating the interfaces within these phases to elucidate their interrelationships. This quasicrystal-like material within an aluminum matrix, characterized by translational symmetry, demonstrates potential for mass production and merits further exploration through AM processes.

Table 1

Parameters of the LPBF process.

Laser Power	Scanning Speed	Beam size	Hatch Space	Layer Thickness
300 W	700 mm/s	35 μm	100 μm	30 μm

Table 2

Composition of designed aluminum-based material.

Element	Al	Ni	Cu	Fe
Wt.%	Balance.	4.0 ± 0.2	2.1 ± 0.1	0.7 ± 0.1
Element	Cr	Mn	Zr	Sc
Wt.%	0.7 ± 0.1	0.7 ± 0.1	0.2 ± 0.15	0.16 ± 0.04

2. Materials and methods

2.1. Materials preparation

The Al-matrix (Al-Ni-Cu) alloy material was fabricated through pre-alloyed powder provided by Circle Metal Powder Co., Ltd., manufactured through electrode induction melting inert gas atomization. ANJI Technology Co., Ltd supports the technical aspects of laser powder bed fusion (LPBF). The composition and print parameters are outlined in Table 1 and Table 2, respectively [47]. The powder SEM appearances are demonstrated in Fig. 1(a), with no significant precipitation on the powder surface, mainly spherical. The process should apply higher laser power to reach specimens without structural defects. The pre-alloyed powder observed by a field-emission scanning electron microscope (SEM, HITACHI SU-5000, Japan) confirmed that the powders mainly present a spherical appearance with an average diameter of 20 μm (Fig. 1(b)). No significant precipitated phase was observed on the powder surface. It was confirmed in Wide-Angle X-ray Scattering (WAXS, D8 DISCOVER with GADDS, Bruker AXS GmbH, Karlsruhe, Germany, CuKα, Beam size: 1.0 mm, working distance: 15.03 cm, with detector Vantec-2000) that the Al-matrix was the primary phase and contained a small amount of Al_9FeNi precipitation (Fig. 1(c)), Al_9FeNi fitting refer to Inorganic Crystal Structure Database#158246 PDF 01-076-2701). The specimen was printed at a 67.3° rotational degree strategy in the LPBF process, primarily to mitigate thermal accumulation and avoid the keyhole mode, reaching the As-printed with no apparent defects. The schematic of Fig. 1(d) depicts the printed strategy of LPBF and shows the laser scanning on the substrate (AA 6061). The as-printed specimen appearances have no apparent printing cracks (Fig. 1(e)). Through additive manufacturing, it is easy to realize customized engineering applications with high dimensional accuracy, which makes repeatable and quantitative production of materials with rational approximant phases feasible. For element diffusion, long-term annealing and air-cooling were performed at an atmospheric pressure of 580 °C for 24 h. After heat treatment, the specimens did not produce macroscopic defects, and further microstructural investigations were introduced.

2.2. Microstructural characterizations

Microstructure was conducted through a high-resolution transmission electron microscopy (HR-TEM, JEOL-2100F, Acceleration voltage: 200 kV) equipped with selected area electron diffraction (SAED) and nano-beam electron diffraction (NBED, electron probe confined in approximant 1 nm) for diffraction modes. Atomic-resolution images were acquired through scanning transmission electron microscopy (STEM) with probe Cs-corrector for high-angle annular dark field (STEM-HAADF, taken an annular-type detector with convergence angle 41 mrad) and complementary bright-field (STEM-BF) detector. Energy disperse X-ray spectroscopy (STEM-EDS) was a windowless silicon drift detector (Oxford Aztec Ultim MAX) used in element quantification and

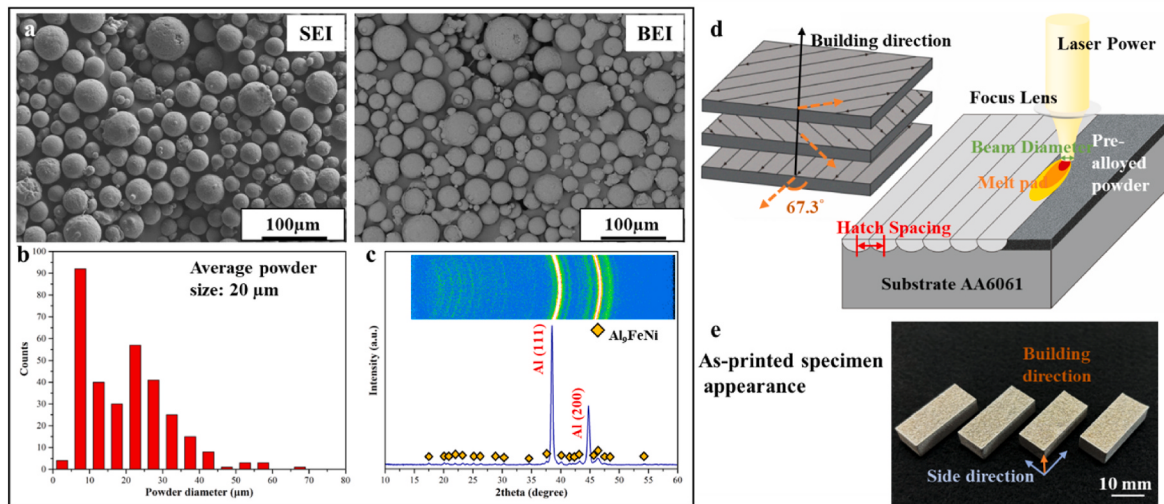


Fig. 1. As-printed specimen preparation. (a) The SEM of the pre-alloyed powder with secondary electron and back-scattered electron images. (b) The powder particle size distribution, where the average particle size is 20 μm . (c) The powder wide-angle XRD shows that the powder mainly contains Al-matrix and trace Al₉FeNi. (d) The schematic of Laser powder bed fusion (LPBF) and rotating the scanning direction by 67.3° along the build direction, and the right schematic depicts the printed parameters. (e) The appearance of the as-printed specimen with no macro-defects.

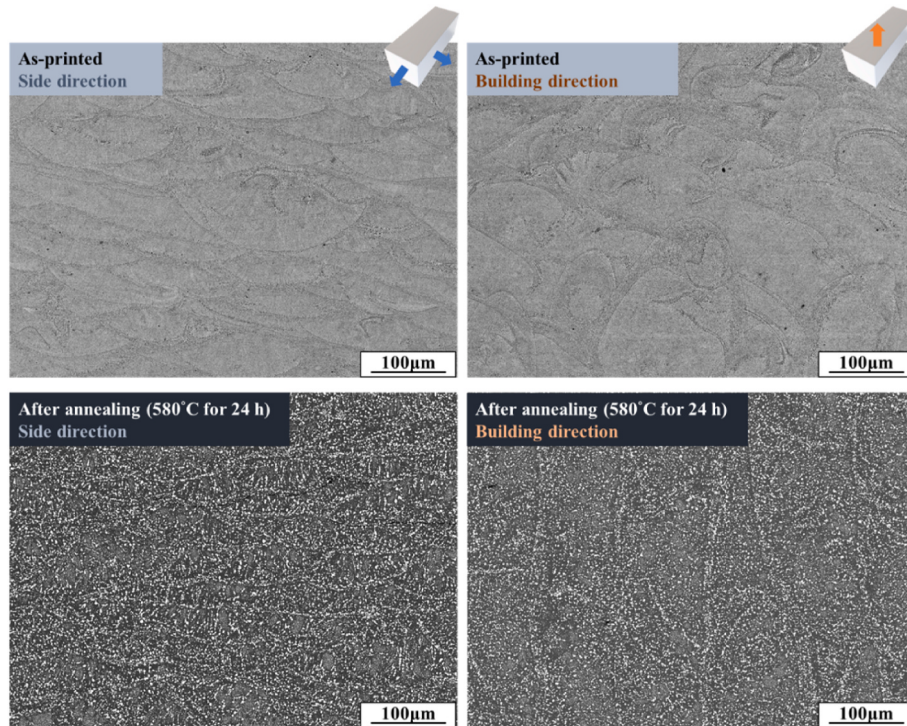


Fig. 2. Microstructure of long-term annealing effects. The SEM-BEI presented the morphology before and after long-term annealing. Before heat treatment, the typical melting pool stacking up layer was confirmed. After heat treatment, the melting pool boundaries decomposed, and precipitation Al₉FeNi grew.

mapping. Electron energy loss spectroscopy (EELS, Exposure: 2S, Acquisition: 20 frames, energy-loss: 48ev, Dispersion: 0.1 ev/ch, Aperture 2 mm) was acquired in the 3–5 different grains of Al₉FeNi and rational approximant phase to reach the typical K-Shell spectrum, respectively. Gatan-Digital-Micrograph software was employed to extract and parse TEM data. For TEM preparation, the specimens were ground with sandpaper, polished with Al₂O₃ and SiO₂, and a focused ion beam (FEI Nova 200, USA) was applied to final preparation to less than 50 nm thickness. In addition, the field emission electron probe micro-analyzer (EPMA, JEOL JXA-8900R, Taipei, Taiwan) was used to investigate the distribution of elements and back-scatter electron image (BEI)

and secondary electron image (SEI).

2.3. X-ray diffraction spectroscopy investigation

Specimens were polished with Al₂O₃ and SiO₂ to a thickness less than 100 μm for XRD of small-angle X-ray scattering (SAXS, NANOSTAR U SYSTEM, Bruker AXS GmbH, Karlsruhe, Germany) and wide-angle X-ray diffraction spectrum (WAXS, D8 DISCOVER with GADDS, Bruker AXS GmbH, Karlsruhe, Germany). CuK α (1.54184 Å) with beam size 1.0 mm served as the source, and Vantec-2000 was used in both instruments (14 × 14 cm² area and 2048 × 2048 pixels density).

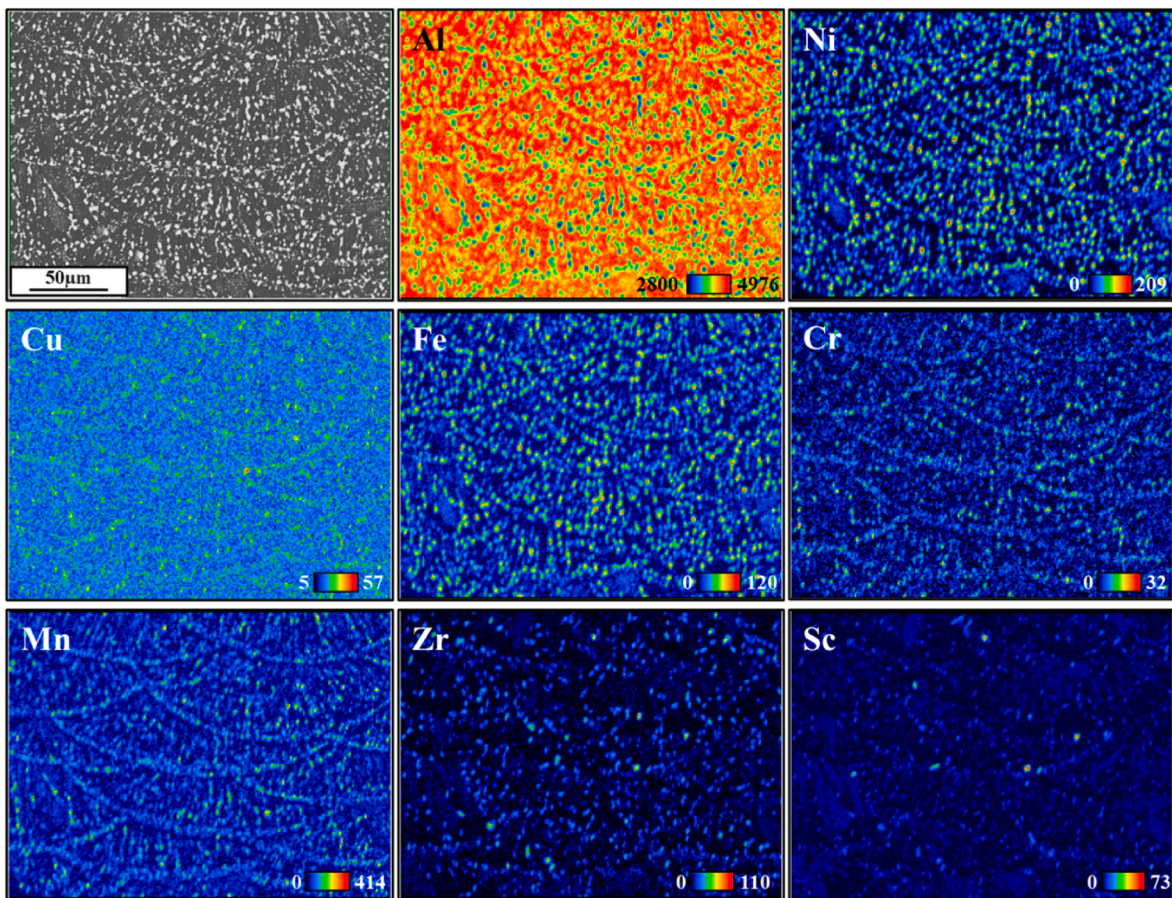


Fig. 3. Elements distribution mapping after annealing. This mapping elucidates the phase composition in the annealed sample, and the detected intensity of elements is indicated. Predominant phase Al_9FeNi is delineated by the overlapping of Al, Ni, and Fe signals, while the presence of the $\text{Al}_3(\text{Zr}, \text{Sc})$ phase is inferred from the co-localization of Al, Zr, and Sc. Additionally, the arc shape of overlapping six elements suggests forming a senary system overlapping.

Single crystal X-ray diffraction structural analysis was introduced to confirm the rational approximant phase. Single crystals were selected for indexing and data collection on a Bruker D8 Venture PHOTON III diffractometer irradiated with graphite-monochromatized Mo K radiation ($=0.71073 \text{ \AA}$). Data integrations and empirical absorption corrections were performed using the APEX 3 software, and crystal structure

was solved and refined using the SHELXTL program. Based on the observed structure factors' intensity distributions and systematic absences, the space group was determined to be $C2/m$ (no.12). In the final refinement cycle, all the atoms were anisotropically refined, and the values of $R1$ and $wR2$ converged to 0.0445 and 0.1292, respectively.

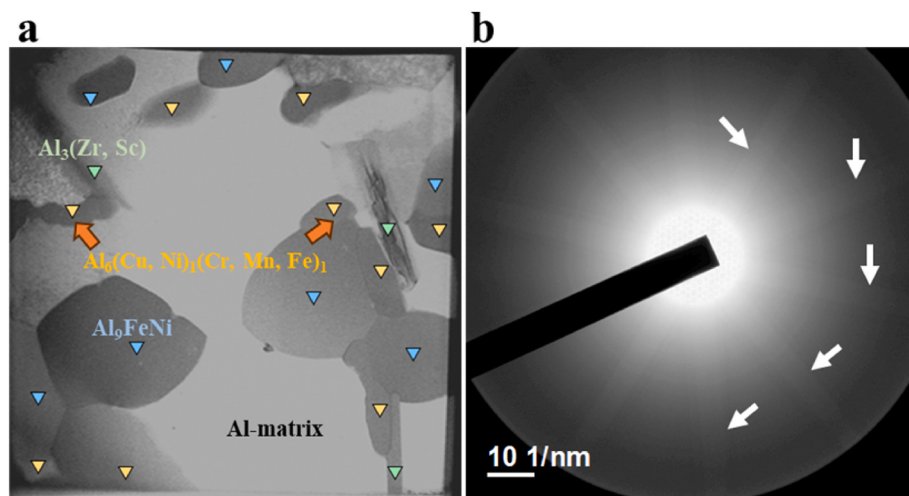


Fig. 4. Phase Distribution in STEM-HAADF Imaging. (a) Through high-angle annular dark-field scanning transmission electron microscopy (STEM-HAADF), the distinct phases within the alloy can be discerned. The dark contrasts represent the Al_9FeNi , $\text{Al}_3(\text{Zr}, \text{Sc})$, and $\text{Al}_6(\text{Cu}, \text{Ni})_1(\text{Cr}, \text{Mn}, \text{Fe})_1$ phases. (b) The Kikuchi pattern presents the pseudo-five-fold rotational symmetry of the rational approximant phase.

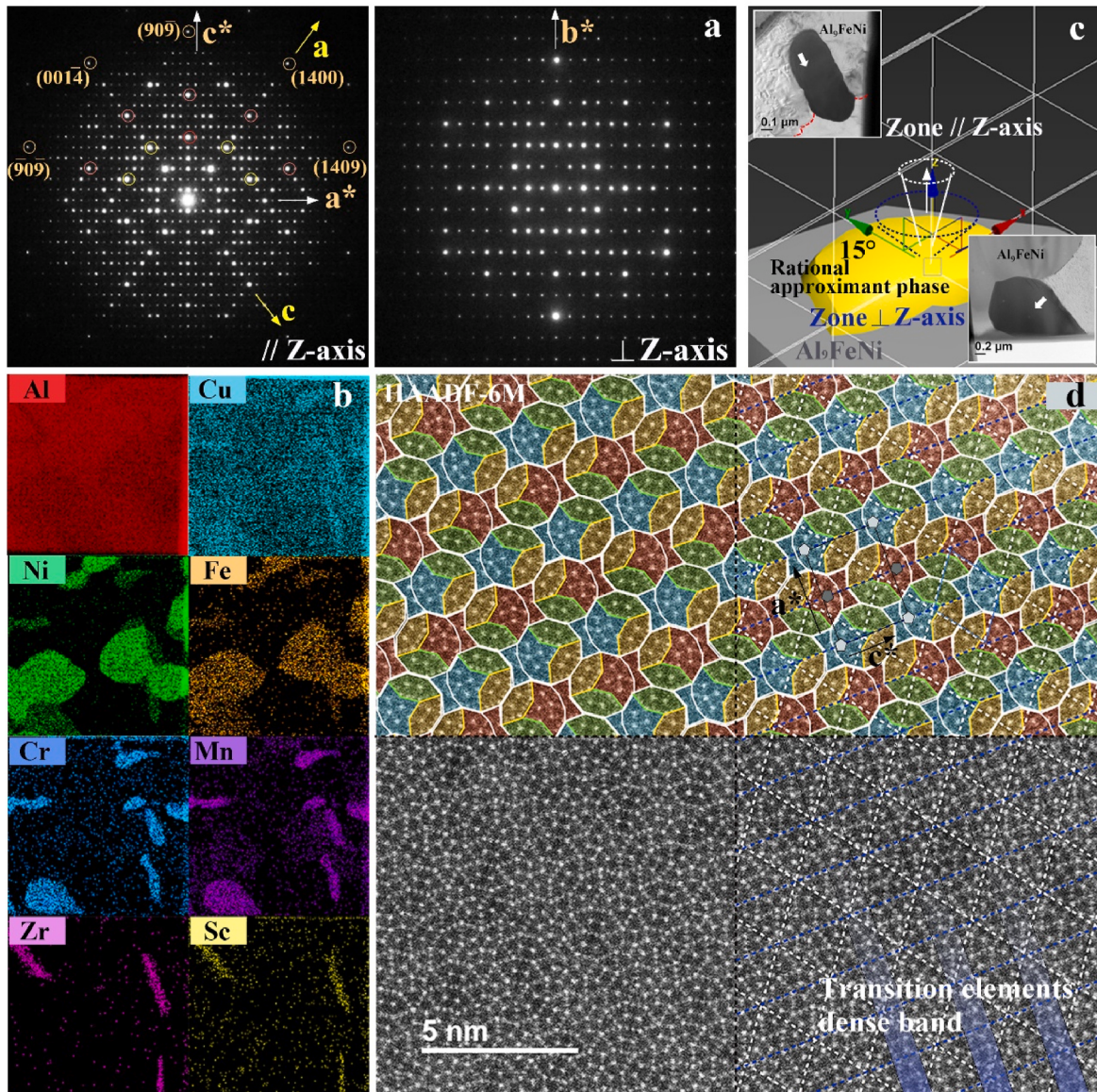


Fig. 5. Tile-Mode Quasicrystal-like Rational Approximant Phase Characteristics. (a) Selected area electron diffraction (SAED) patterns display the pseudo-five-fold symmetry axis (left) and two-fold symmetry axis (right), with zone axes oriented dependent on Al₉FeNi sites. (b) Elemental distribution is verified by STEM-EDS mapping, highlighting the composition of each phase. (c) A schematic representation illustrates the alignment of different quasicrystal zone axes with the Al₉FeNi phase. (d) High-angle annular dark-field (HAADF) imaging at atomic resolution reveals the tessellated periodic arrangement of quasicrystal-like rational approximant structural blocks, with no arranged defects within. Additionally, the HAADF image unveils the sublattice with bands of high-density transition elements (linked by the centers of Star-sublattices and their surrounding atoms) creating an interlaced pattern of periodic bright and dark bands, subsequently referred to as TEDB.

3. Results

3.1. Senary system rational approximant phase with quasi-periodic rotational symmetry

The morphologies of Al–Ni–Cu–Fe–Mn–Cr alloy before and after long-term annealing (580 °C for 24 h) are demonstrated through SEM-BEI (Fig. 2). Before heat treatment, typical melting pool stacking up layers were confirmed and divided into columnar-grained and fine-equiaxed-grained regions. After heat treatment, the melting pool boundaries decomposed, and secondary phases grew in these original regions. EPMA analysis elucidated the micro-distribution of elements within the alloy (Fig. 3), confirming the composition and distribution of secondary phases. Regions enriched in Al–Ni–Fe correspond to the Al₉FeNi phases, while Al–Zr–Sc rich domains suggest the Al₃(Zr, Sc)

phases. Furthermore, the overlapping distribution of a six-element system involving Al–Ni–Cu–Fe–Mn–Cr reveals heterogeneity related to the Al₉FeNi phase, particularly forming an arc-like distribution trend in the vicinity of the original melting pool boundaries. Research efforts continue to probe the complexities of this senary system, with a targeted analysis toward arc-shaped regions. Confirmed through transmission electron microscopy bright field (BF) image and scanning transmission electron microscopy energy-dispersive X-ray spectroscopy (STEM-EDS), it is confirmed that the alloy comprises four distinct phases: Al matrix, Al₉FeNi, Al₃(Zr, Sc), and quasicrystal-like rational approximant phase Al₆(Cu, Ni)₁(Cr, Mn, Fe)₁ (Fig. 4(a), and Table 1). The Kikuchi pattern observed in Fig. 4(b) of this rational approximant phase under TEM diffraction mode suggests a pseudo-five-fold rotational symmetry reminiscent of quasicrystals. The orientation distribution of the Al₉FeNi zone axis shows a strong correlation with the position of the rational

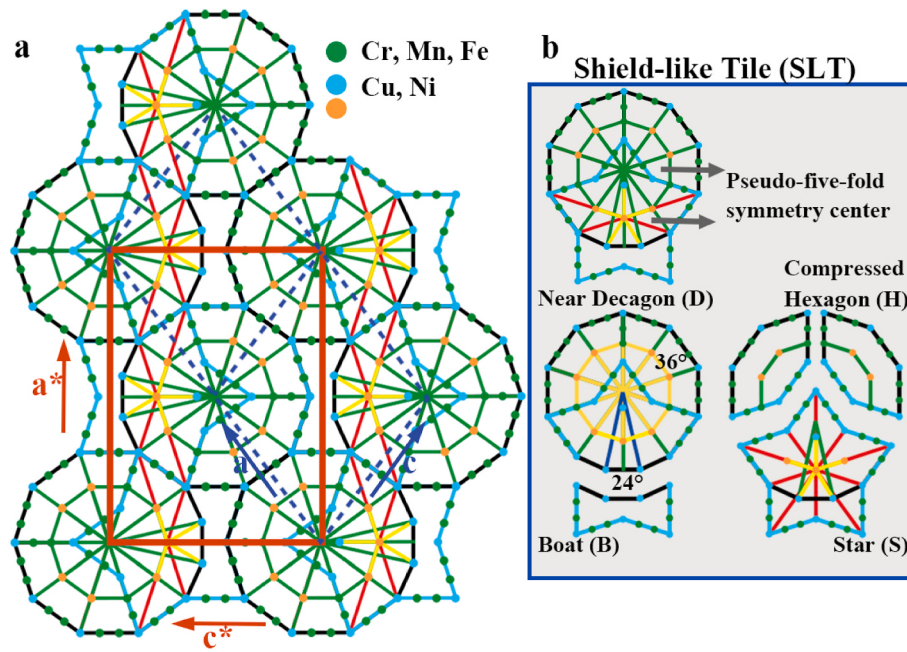


Fig. 6. Illustration of Rational Approximant Phase Atomic Structure and Sublattice Division. (a) Displays the atomic arrangement featuring a Fibonacci approximant orthorhombic lattice in red, interlaced with an observed rhombus lattice in blue, highlighting the positions of transition elements (Cr, Mn, Fe) and (Cu, Ni). (b) The SLT is divided into four sublattices through different quasi-rotational symmetry centers—Near Decagon (D), Compressed Hexagon (H), Boat (B), and Star (S). (For interpretation of the references to colour in this figure legend, the reader is referred to the Web version of this article.)

phases, as schematically represented (Fig. 5(a)-(c)). When the zone axis aligns nearly parallel to the z-axis, a quasi-periodic diffraction pattern becomes evident (the zone axis is the same as the Kikuchi pattern in Fig. 4(b)), with the pseudo-five-fold symmetry zone axis observed near the transmission beam. In contrast, orientations closer to the vertical predominantly reveal two-fold zone axes. In Fig. 5(c), the top part reflects a pseudo-five-fold axis from Fig. 5(a)-left, and the bottom part displays a two-fold axis from Fig. 5(a)-right, demonstrating the influences of phase distribution and the zone axis orientation. The fundamental unit of pseudo-five-fold selected area electron diffraction (SAED) (Fig. 5(a)) corresponds to two-fold approximate ($a^* = 3.22 \text{ nm}$, $c^* = 2.37 \text{ nm}$). Fibonacci approximants within an orthorhombic lattice (F_n/F_{n-1} , F_m/F_{m-1} , with the Fibonacci sequence: 0, 1, 1, 2, 3, 5, 8 ..., F_n ; $F_{n+1} = F_n + F_{n-1}$) are employed to approximate the lattice as $(3/2, 2/1)$. The distances of intense diffractions along one direction are 3, 5, 8, and 13 units, while on the other axis, they are 2, 4, 6, 10, and 16 units, corresponding to the Fibonacci number sequence. Therefore, this lattice approximates the irrational number. To further illustrate the periodic lattice characteristics of these rational approximant phases, monoclinic lattice calibration was applied, setting the Fibonacci approximant orthorhombic lattice parameters a^* to [10-1]; c^* to [101] ($a = 1.92 \text{ nm}$, $c = 1.92 \text{ nm}$, $\gamma = 108^\circ$, monoclinic). While the pseudo-five-fold rotational symmetry is a dominant feature in typical DQCs [48,49], achieving a two-fold zone axis in this rational approximant phase is crucial for the pseudo-five-fold diffraction points to exhibit strong diffraction intensity. Consequently, due to this unmet structural condition, the innermost pseudo-five-fold diffraction points along the c^* axis show weak diffraction values. Furthermore, the diffraction pattern on the [010] zone axis, which bears a resemblance to that of Robinson phase (R-type) $C_{31}-Al_{60}Mn_{11}Ni_4$ [50–52], the outermost pseudo-five-fold diffraction points in this rational approximant phase exhibit faint diffraction values. The diffraction of rational approximant structures can be interpreted as an amalgamation of periodic and quasiperiodic structural features, comprising a periodic lattice (superlattice) and a quasi-periodic arrangement (fundamental lattice). The resulting diffraction pattern emerges from the interplay between these two structures: the superlattice determines the primary array of the

diffraction pattern. In contrast, the basic structure influences the intensity distribution of the spots. Thus, the diffraction pattern in rational approximant structures can be seen as a convolution of the superlattice's sharp peak functions with the Fourier transform from the basic structure [52].

3.2. Quasicrystal-like rational approximant with defect-free

The STEM-HAADF technique reveals the rational approximant structure along the pseudo-five-fold zone axis (Fig. 5(d)) with lattice arrangements marked by the white line. The structure, $Al_6(Cu, Ni)_1(Cr, Mn, Fe)_1$, comprises two primary sublattices: star-shaped (S) and compressed hexagonal (H), both free of apparent arrangement defects [53]. Differing from overlapping modes observed in Gummelt and Lück quasicrystal structures, there's no indication of a three-dimensional overlapping interval among these rational approximant structural blocks. As shown in Fig. 6(a), these sublattices do not overlap; instead, they adjoin one another, sharing edges. The S sublattices (blue S-red S-blue S ...) connect along a single edge, akin to the Al-Cr-Fe-Si system [54–57], thereby being the tile mode applied for further explanation. Fig. 6(b) illustrates that a single S sublattice with two H sublattices forms a shield-like tile (SLT), which can also be visualized as a fusion of an 11-sided structure (D) and a near-dumbbell shape (B). This distinct S sublattice, boasting five additional atoms around the S center atom, sets it apart from typical DQCs. Moreover, the outer atomic arrangement of the D sublattice does not perfectly correspond to regular decagons, where the standard 72° angle of the D sublattice should evenly divide into 36° in a standard decagonal structure. Instead, the presence of additional S atoms splits it into three segments (24°). It is worth noting that an extra internal layer of the five-fold atomic arrangement (yellow in Fig. 6(b)) is observed within the D sublattice. This unique SLT constitution diverges from previously reported types [45]. The structure exhibits translational symmetry along the c^* axis, with a distinct pattern where the orientation of the sublattice arrangement alternates row by row, leading to staggered shield-like tiles (SLTs) along the a^* direction, occurring periodically as shown in Fig. 6(a). This feature aligns with the characteristics of rational approximants, which maintain translational

Table 3

STEM-EDS element quantitative analysis of different phases. Each atomic percentage (at. %) is obtained through the average of 3 or more grains, and the ratio of (Ni, Cu): (Fe, Mn, Cr) = 1:1 is regarded in the HAADF imaging atomic arrangement. This phase is thus defined as $\text{Al}_6(\text{Cu}, \text{Ni})_1(\text{Cr}, \text{Mn}, \text{Fe})_1$.

Element	Al	Ni	Cu	Fe	Mn	Cr	Zr	Sc
Al matrix	96.7	—	3.1	—	—	0.2	—	—
Al_9FeNi	74.7	15.3	6	3.1	0.7	0.2	—	—
$\text{Al}_3(\text{Zr}, \text{Sc})$	72	0.1	7.3	—	—	0.3	16.7	3.6
Rational approximant phase	74.7	4.2	8.3	0.8	5.8	6.2	—	—
Nanolayered phase	74.4	4.2	20.0	0.9	0.3	0.3	—	—

symmetry even while exhibiting quasi-periodic-like structural aspects such as pseudo-five-fold rotational symmetry. Similar sublattice arrangements in HAADF have been reported previously [16], but this specific phase's inclusion of different SLT types introduces complexity in

maintaining equivalent periodicity over long-range orders. This observation suggests that involving multiple SLT types may be more restricted than quasicrystals for forming a rational approximant. Such a factor could be crucial in establishing the rational approximant structure, emphasizing the need for fixed sublattice configurations and fewer sublattice types to achieve translational symmetry. In contrast with other quasicrystals, a notable distinction of this rational approximant is the evident dark line of Al atomic arrangement visible in HAADF, which slices through the centers of all D sublattices, presenting as rhombus-like structures. Each set of dark lines, indicated as dashed white lines in Fig. 5(d), evenly divides the H sublattices, both yellow H and green H, into two halves, with the c^* axis serving as the mirror symmetry axis for the S sublattices. Combining any two adjacent triangles creates a parallelogram or rhombus along the c^* axis, and these sets of dark lines form the basis for a completely equivalent periodic lattice structure. These lines correspond to the [100] and [001] axes, locations of strong diffraction (Fig. 5(a)). Furthermore, this quasicrystal-like structure's

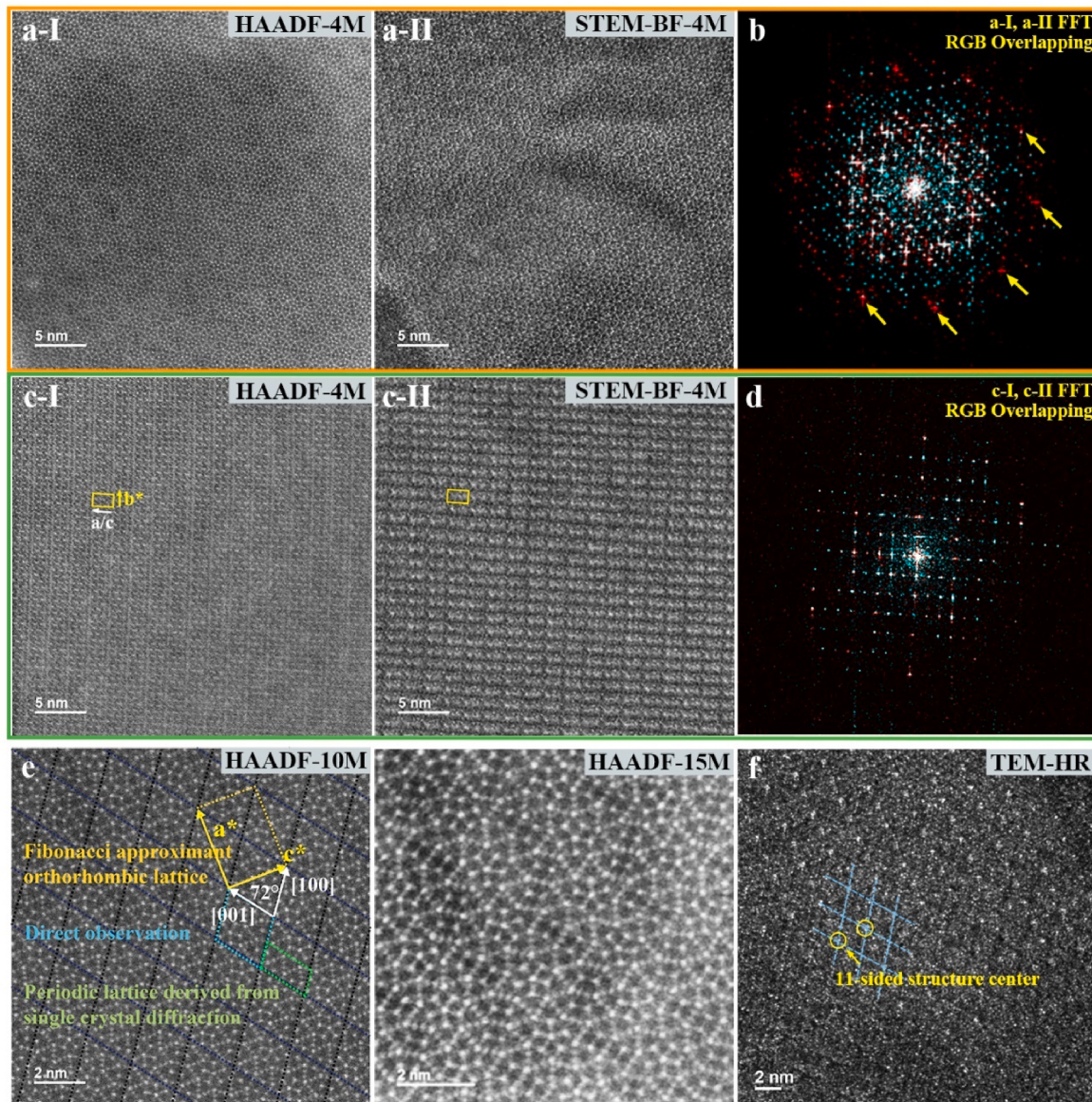


Fig. 7. Manifestation of Rational Approximant Cluster Monomer in Long-Range Ordered Periodic. (a)(b) Atomic-resolution STEM-HAADF images along the pseudo-five-fold axis display periodicity at low magnification along the corresponding STEM-bright field image. The combined FFT RGB overlay highlights the pseudo-five-fold and the two-fold symmetry. (c)(d) Under identical imaging conditions but along the two-fold axis, comprised of b^* and [100]/[001], with RGB overlaps. (e) The HAADF image shows the basic equivalent periodic lattice framed naturally by black lines, with the highest HAADF image detailing the lattice (f) High-resolution TEM images further illustrate the periodic arrangement of monoclinic boundaries and the center of D-sublattice within this rational approximant phase.

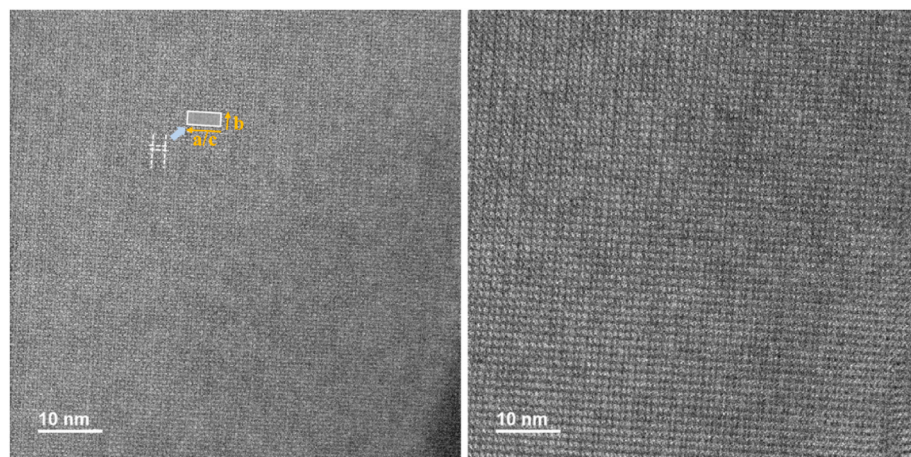


Fig. 8. Periodic defect-free at Low Magnification. Low-magnification imaging reveals the quasicrystal's lattice along the b-axis (equivalent to b^*) in STEM-HAADF (left) and STEM-BF (right). The images highlight a defect-free periodic lattice.

Fibonacci approximant orthorhombic lattice aligns with the space group $Pmmn$ [50]. However, it is essential to note that the equivalent periodic lattice, indexed by the Fibonacci approximant, may not be the most fundamental periodic unit cell, as directly indicated by the monoclinic

lattice observed in HAADF (Fig. 6(a)).

STEM-EDS analysis evidences that the primary constituents of the quasi-periodic structure are transition elements (Table 3), including Cu, Ni, Cr, Mn, and Fe. Cu and Ni form the primary sublattice framework in

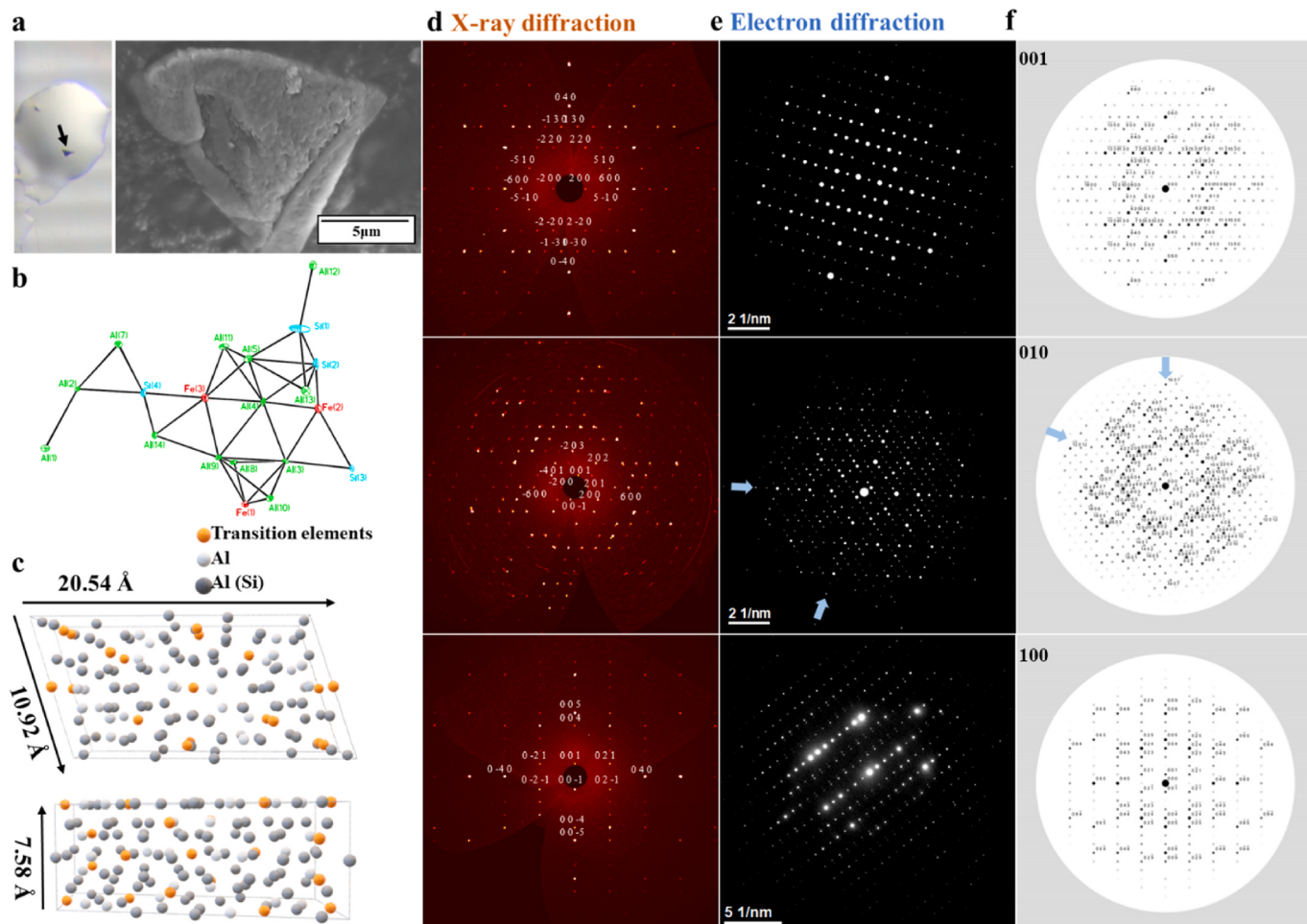


Fig. 9. The Rational Approximant Lattice Analyzed through Single-crystal X-ray Diffraction. (a) Optical and SEM images reveal the hardness-derived single crystal. (b) Depicts the atomic arrangement of the base monomer. (c) Showcases the periodic unit lattice and atomic arrangement derived through single crystal X-ray diffraction. (d)(e) X-ray diffraction patterns along the a-, b-, and c-axes correlate with selected area electron diffraction (SAED). (f) Theoretical diffraction patterns calculated from the X-ray-derived structure illustrate the zone axis projections, offering a comparative reference to empirical SAED results.

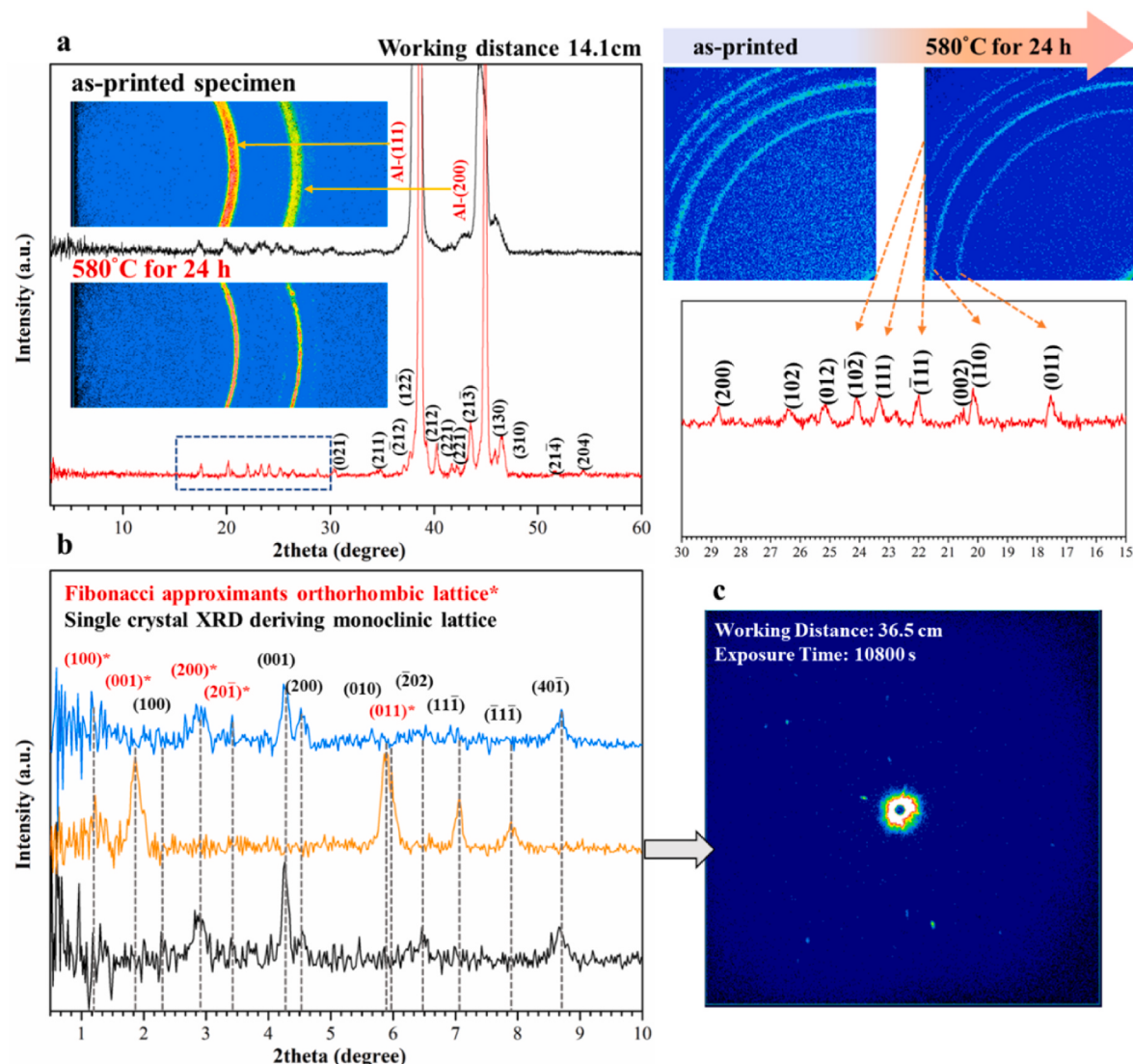


Fig. 10. X-ray Diffraction Analysis for Phase Identification in Engineering. (a) Wide-angle XRD indicates enhanced crystallinity in both the Al matrix and Al₉FeNi phase after annealing, implying the diffusion of solid-solution elements. (b) Small-angle XRD in transmission mode results demonstrated angles <10° at different locations display the rational approximant phase diffraction. Despite Al₉FeNi peaks obscuring signals above 15°, these diffraction peaks are distinct at smaller angles. (C) Long-exposure XRD captures a detailed polycrystalline ring, validating XRD's capability to preliminarily identify the rational approximant phase for engineering applications.

this structure, while Cr, Mn, and Fe are coordinated in HAADF (Figs. 5 (d) and 6(a)). The low-magnification HAADF image incorporates height information, validating this periodic structure's mutually perpendicular lattice frame parameters observed on the two-fold and pseudo-five-fold symmetry zone axes. The lattice parameters are indicative of a monoclinic system ($a = 20.43 \text{ \AA}$, $b = 20.43 \text{ \AA}$, $c = 7.62 \text{ \AA}$, $\alpha = 90^\circ$, $\beta = 90^\circ$, $\gamma = 107.9^\circ$). The observation in this structure is translational symmetry combined with a defect-free lattice, corroborating the tile mode arrangement in a three-dimensional framework (Fig. 7(a)-(d)). The complementary fast Fourier transform (FFT) analysis of STEM-HAADF (red) and bright field (BF) images (blue) are combined using RGB layers to offer a comprehensive view. The FFT underlines the orderly and structured nature of the rational approximant phase. In this representation, it is evident that Al atoms play a dominant role in establishing the periodic structure. Meanwhile, the quasi-fold diffraction patterns are primarily influenced by the added transition elements. Al atoms fulfill the coordination of transition elements and involve the black rhombus lattices. The vertices of these rhombus lattices align with the centers of the D sublattices (Fig. 7(e)-(f)). Further insight is provided by high-

resolution transmission electron microscopy (HR-TEM) imaging (Fig. 7 (f)), showing that the D centers, characterized by stronger phase contrast, exhibit translational symmetry, leading to an orthorhombic array.

3.3. Rational approximant structure confirmed through X-ray diffraction

As demonstrated in Fig. 8, lower magnification STEM imaging provides insight into the lattice arrangement of the rational approximant along the b-axis. With its stacking-up configuration, this tile mode lattice exhibits a defect-free structure characterized by periodic-equivalent features, highlighting the stability and periodic nature of the rational approximant. This study verified these natures using single-crystal X-ray diffraction (SXRD), providing solid crystallographic evidence of its ordered and periodic lattice structure. Through hardness difference, a single crystal with rational approximant characteristics was extracted (Fig. 9(a))). The lattice information obtained from single-crystal analysis aligns with the electron diffraction results. The rational approximant structure derived via SXRD in Fig. 9(b)-(c) exhibits the atomic

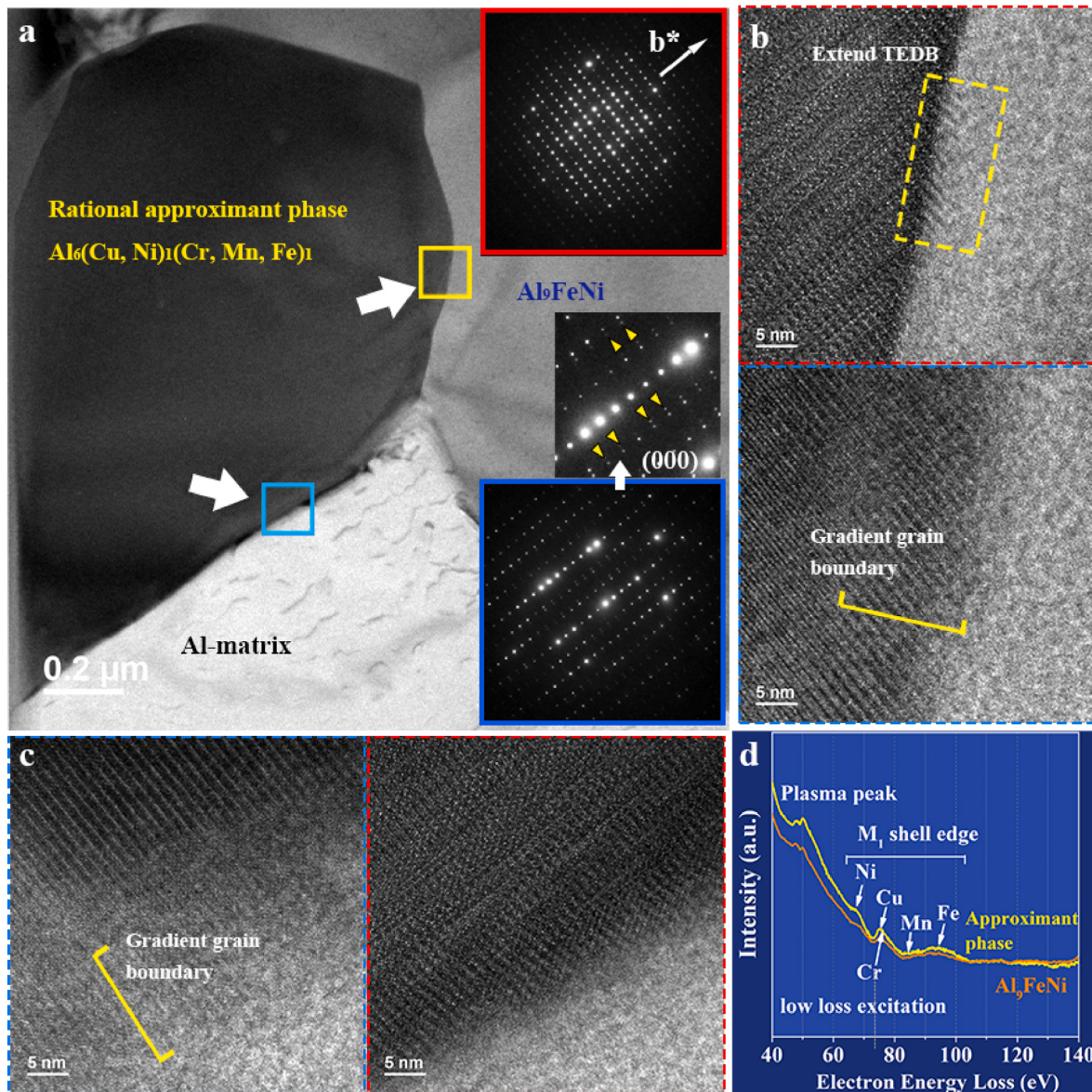


Fig. 11. The Boundary Coherence with Al_9FeNi and Al Matrix. (a) The bright-field TEM image reveals the rational approximant phase in contact with the Al_9FeNi and Al matrix, where selected area electron diffraction (SAED) indicates lattice distortion near the boundary (yellow triangle). (b)(c) High-resolution TEM provides a closer look at the coherent interface between the approximant phase and Al_9FeNi and between the approximant phase and the Al lattice, across different orientations. (d) Electron energy loss spectroscopy (EELS) spectra suggest that the approximant phase and Al_9FeNi share similar elements' configurations. (For interpretation of the references to colour in this figure legend, the reader is referred to the Web version of this article.)

arrangement of the monomeric unit and its corresponding periodic unit lattice. This foundational monomeric unit provides a tangible representation of the translational periodic characteristics, displaying the orderly arrangement of transition elements and coordinated Al atoms, with bond lengths indicating their spatial relationships (Transition elements represented by Fe atoms, and Si positioning derived from software may indicate significant distortion among Al atoms). The derived lattice parameters are monoclinic: $a = 20.57 \text{ \AA}$, $b = 10.94 \text{ \AA}$, $c = 7.59 \text{ \AA}$, $\alpha = 90^\circ$, $\beta = 90^\circ$, $\gamma = 107.6^\circ$, within the space group C 2/m. The diffraction patterns observed through SXRD exhibit clear correspondences with those identified through electron diffraction, as demonstrated in Fig. 9 (d)–(f) by comparing angles and interplanar spacings across primary zones. While SXRD along the quasi-fold ($h0l$) orientation provides significant insights, it does not fully capture the quasiperiodic rotational symmetry. As a result, the derived lattice parameters may not fully encompass quasicrystal-like features. Nonetheless, the crystal volume, determined as half of that observed in HAADF (Fig. 7(e)), is insightful

for rational approximants. This provides a reference framework for identifying structures with quasicrystal-like rational approximant phase characteristics in practical engineering applications, establishing a foundation for their wider use in industries.

Wide-angle X-ray diffraction (XRD) analysis, as depicted in Fig. 10 (a), suggests that lattice deformation within both the aluminum matrix and Al_9FeNi phases diminishes post-annealing. However, diffraction peaks beyond 15° become obscured by the Al_9FeNi phase, making the rational approximant structure signals indistinguishable at these higher angles and prone to being dismissed as background. Notably, within the narrow scope of angles less than 10° by small-angle XRD employing transmission mode with a prolonged exposure time of 3 h, the peaks of the rational approximant structure emerge unobscured, as shown in Fig. 10(b)–(c). These peaks, distinguishable from the Al matrix and Al_9FeNi phase due to significant d-spacing differences, remain unaffected by adjacent phases. The peaks marked in black correspond to the monoclinic lattice, as established through single-crystal diffraction. In

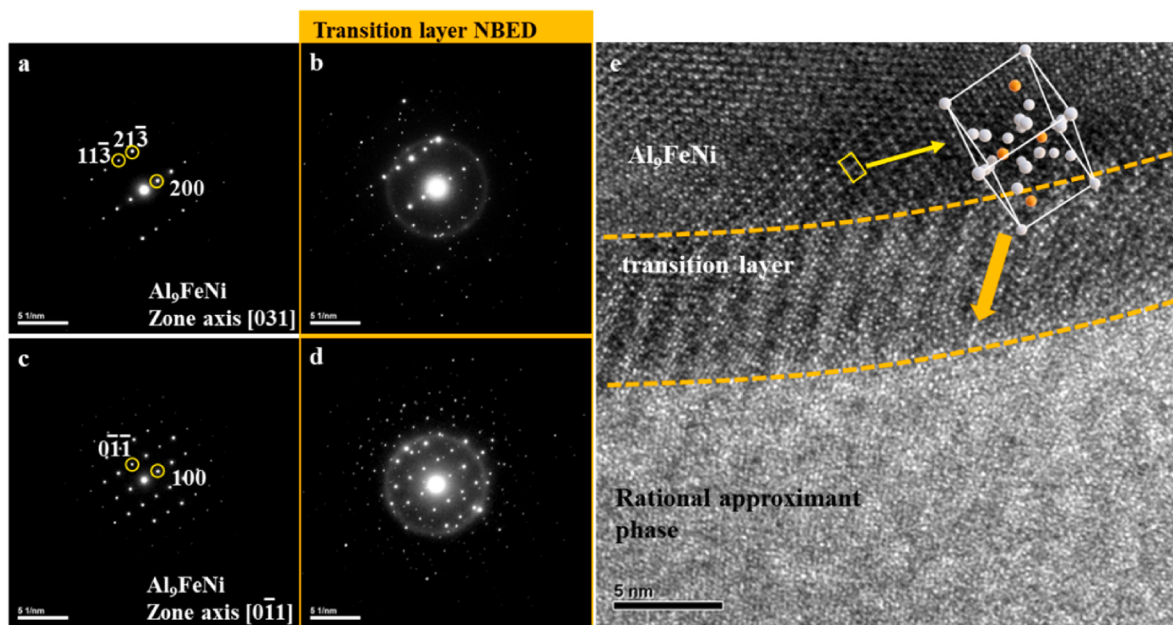


Fig. 12. The Interfacial Characteristic of Al_9FeNi and Rational Approximant Phase. (a)(b) Display SAED patterns and nanobeam electron diffraction (NBED) adjacent and on the transition layer along the Al_9FeNi zone axis [031]. (c)(d) Show corresponding SAED and NBED patterns along the Al_9FeNi zone axis [$0\bar{1}1$], highlighting the lattice transitions. (e) The HR-TEM image of $[0\bar{1}1]$ accentuates a distinct transition layer.

contrast, the red peaks indicate the orthorhombic translational symmetry of rational approximants derived from electron diffraction Fibonacci approximants. These findings demonstrate the feasibility of using X-ray diffraction to identify rational approximants as a preliminary tool for confirming the formation of such structures in engineering applications.

3.4. Phase boundary coherency of rational approximant phase

While the formation mechanism of quasicrystals within the realm of additive manufacturing remains an underexplored area, studies explicitly targeting the formation of rational approximant structures are even more scarce. A comprehensive understanding is still pending further research, and evidence suggests that the formation process is closely linked to the diffusion of elements within a supersaturated solid solution, which emerges under high solidification rates. Furthermore, the genesis of rational approximant phases may be closely related to the mechanisms of phase transformation from quasicrystal to crystalline structures during the heat treatment. The high cooling rates inherent in AM promote the formation of supersaturated solutions and metastable phases, essential for developing quasicrystals and their approximants. Subsequent heat treatments further contribute to stabilizing and enhancing these materials' performance. Addressing these challenges, this study delves into the distribution of elements, grain boundary characteristics between rational approximants and surrounding phases, and orientation distribution to elucidate the phase transformation mechanism into rational approximants. The notable rational approximant structure identified in this study did not manifest immediately after 1-h annealing at 580 °C but became apparent after 24 h [40]. Initially, elements like Cr and Mn were predominantly in a solid solution within Al_9FeNi . This can be attributed to the thermodynamic stability of Al_9FeNi , which is pivotal in governing the phase transformation process leading to the formation of the $\text{Al}_6(\text{Cu}, \text{Ni})_1(\text{Cr}, \text{Mn}, \text{Fe})_1$. STEM-EDS mapping corroborates the gradual diffusion progression of Cr and Mn between Al_9FeNi and the rational approximant, as well as between the rational approximant and Al, which are coherent, as depicted in Fig. 11(a). These coherent interfaces facilitate favorable atomic interactions. The coherent grain boundary clearly delineates the two phases along the

[010] axis of the rational approximant. Strikingly, several layer stripes extend from the rational approximant to the Al_9FeNi phase across this boundary, as shown in Fig. 11(b)–(c). These stripes correspond to the sublattice arrangement period of the rational approximant, suggesting a close relation to the transition element dense band (abbreviated as TEDB) within its lattice. These TEDBs, appearing brighter in HAADF, traverse through the central portions of S sublattices, consisting of six atoms arranged around a central one, as indicated in Fig. 5(d). They also extend into Al_9FeNi , indicating that the diffusion of transition elements likely originates from this phase. Additionally, HR-TEM reveals a gradual alteration in the atomic arrangement between the rational approximant and Al_9FeNi along the [100] zone axis, where these stripes become observable. To establish the connection between the two phases, a comparison of transition elements' M-shell electron energy loss spectroscopy (EELS) was conducted (Fig. 11(d)), which reveals similar electronic configurations between the rational approximant phase and Al_9FeNi . Furthermore, on the Al_9FeNi ($0\bar{1}1$) zone axis, the TEDB becomes more pronounced, forming a transition layer (Fig. 12). The nanobeam electron diffraction (NBED) patterns of these stripes suggest that transition elements are progressively forming solid solution structure as superlattice within the Al_9FeNi lattice. This observation might indicate a diffusion remnant during the rational approximant's formation process.

As depicted in Fig. 13(a), the grain boundary between the rational approximant and aluminum is confirmed to be coherent in HAADF imaging. The interface of the rational approximant aligns parallel to the c^* -axis on the pseudo-five-fold axis, with the nearest sublattice layer experiencing minimal lattice deformation and remaining parallel to the interface. Within the aluminum matrix near the rational approximant, SAED reveals a ring pattern with interplanar spacing approximately half that of aluminum's face-centered cubic lattice. Across various zone axes, including 2-, 4-, pseudo-5-, and 6-fold, strong diffraction ring patterns are observed, indicating the rational approximant's ability to maintain coherence with aluminum while exhibiting slight lattice distortion across different orientations (Fig. 13(b)–(c)).

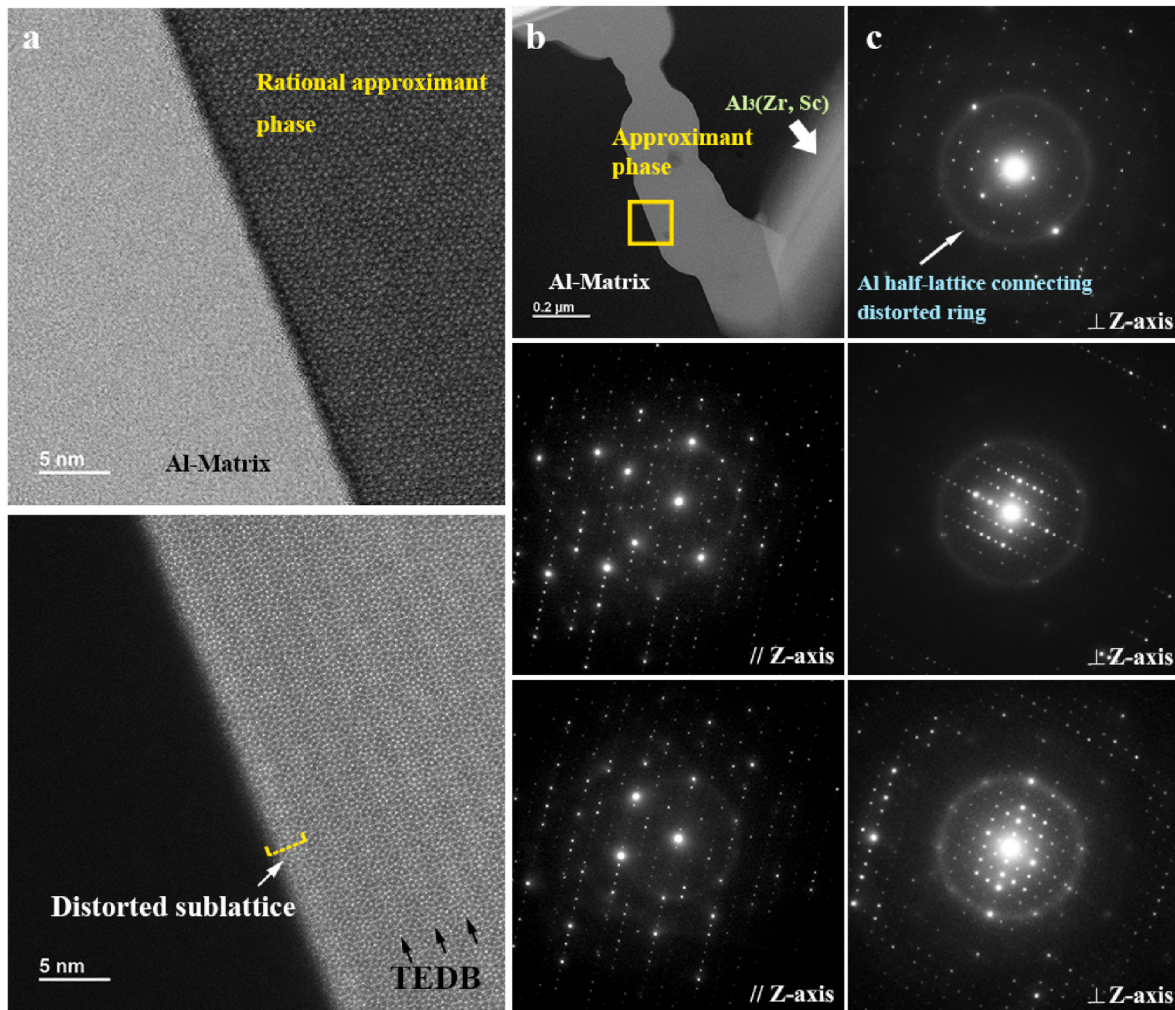


Fig. 13. Boundary Morphology and Coherency between the Rational Approximant Phase and Al Matrix (a) The interface of the rational approximant phase with the Al matrix is shown along the pseudo-five-fold zone axis in atomic-resolution STEM-HAADF and STEM-BF images, showcasing the boundary morphology, where (b) the STEM-HAADF image pinpoints the location. (c) NBED patterns adjacent to the Al boundary suggest the existence of lattice planes that may connect with the Al matrix, indicating that the approximant phase and Al lattice could share coherent relationships on different symmetries.

3.5. Formation mechanism of rational approximant structure

The formation mechanism of the rational approximant phase may be attributed to its capacity to establish bridging coherence along the Al-Al₉FeNi boundary. This coherence aids in reducing the increase in lattice mismatches between Al-Al₉FeNi during grain growth, thereby diminishing phase interfacial energy. Apart from the observed sized rational approximants, there is a distinct presence of thin layered transition phases, only a few nanometers thick, acting as buffers between Al₉FeNi and Al, as shown in Fig. 14(a)-(b), Table 3. Regarding Al₉FeNi, the electron configurations of Cu, Cr, and Mn diverge from those of Fe and Ni. Owing to the rapid solidification rate during additive manufacturing, they become supersaturated and dissolve into the Al₉FeNi lattice. Subsequent to prolonged annealing, the lattice of Al₉FeNi undergoes a migration of Cu, Cr, and Mn outward, reducing lattice distortion. NBED analysis shows that the diffraction characteristics of Al₉FeNi remain prominent within the layered phase, and an additional superlattice of Cu supersaturated solid solution emerges, suggesting the formation of a tile-like characteristic (The atomic arrangement also similar to the tetragonal lattice of Al₃Ni₂, which is the high-temperature non-equilibrium phase). In Fig. 14(a), the layered phase lacks sufficient Cr and Mn—these elements have been consumed by another rational approximant phase on the opposite side of Al₉FeNi, leading to the substitution by Cu and thereby limiting the driving force

for further structural growth. This observed nanolayered phase may be considered as another phase resulting from this phase transformation process. Therefore, it can be inferred that the formation of the rational approximant phase depends on the solubility of Cr and Mn within the original Al₉FeNi lattice. Fig. 14(b) provides a three-dimensional perspective, showing the nanolayered superlattice phase's lattice aligning with Al and Al₉FeNi. Observing atomic arrangement images, the tile-like mode structure becomes apparent in the nanolayered phase. Layered Cu-superlattice planes stack up on the Al lattice between the nanolayered phase and Al, forming a coherent phase boundary.

Fig. 15 of HR-TEM, augmented by FFT analysis, displays a cross-sectional view through the Al₉FeNi phase, the nanolayered phase with a superlattice, and the α -Al matrix. Fig. 15(b)–(c) depicts the transition from the Al₉FeNi phase to the nanolayered phase, where an overlap in the lattices is especially noted within the transition layer. This overlap extends along the nanolayered phase's b-axis, which has a larger d-spacing, as shown in Fig. 15(d). Moreover, this axis's lattice also exhibits coherence with the Al (111) planes, as evident in Fig. 15(e)–(f). The coherence in lattice alignment is pivotal for stabilizing and growing the quasicrystal-like rational approximant structure. Such lattice alignment coherence acts as a crucial driving force in the phase transformation process to stabilize and promote the rational approximant phase and nanolayered phase growth, aiding in regulating the lattice mismatches

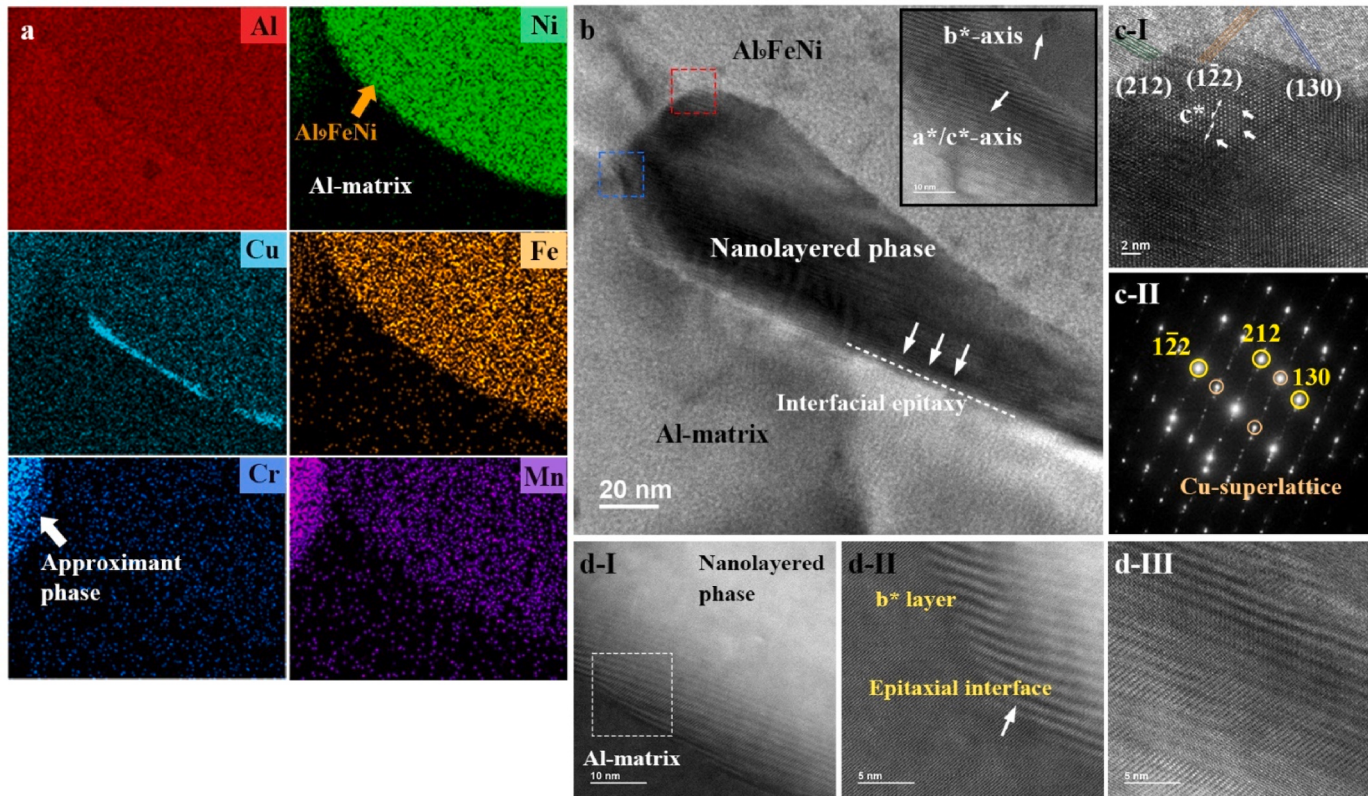


Fig. 14. Interfacial Growth Mechanism of the Rational Approximant Phase. (a) STEM-EDS mapping distinctly reveals the elemental composition at the interface of the nanolayered phase with Al₉FeNi and the Al matrix. The mapping indicates the enrichment of Cr and Mn in the rational approximant phase, whereas the nanolayered phase exhibits a higher concentration of Cu. (b) Bright-field TEM image, showcasing the nanolayered phase, reveals a cross-sectional view that exposes the three-dimensional lattice. This perspective captures two distinct lattice orientations: one interfacing with Al₉FeNi, and another transitioning towards the Al matrix. (c) The HR-TEM image and NBED patterns present the nanolayered phase at the interface with Al₉FeNi (located at the red frame in b). The lattice of the nanolayered phase closely resembles and connects to Al₉FeNi, but the primary distinction is the presence of a Cu superlattice. (d) HAADF imaging (located at the blue frame in b) reveals a layered striation within the nanolayered phase. (For interpretation of the references to colour in this figure legend, the reader is referred to the Web version of this article.)

between the Al matrix and Al₉FeNi. It should be clarified that the nanolayered phase is characterized by the absence of Cr and Mn incorporation. Despite the presence of a layered structure, it does not exhibit a pseudo-five-fold rotational symmetry arrangement in quasi-periodic. However, the formation of this phase may have undergone a diffusion process similar to that of the rational approximant phase. Combining STEM-EDS data and atomic arrangement evidence suggests a transformation in Al₉FeNi involving partial lattice consumption. This leads to the gradual formation of a quasicrystal-like rational approximant phase and evolution at phase boundaries. This partial transformation can be attributed to a higher content of Cr and Mn in the lattice, enhancing coherence with the Al lattice compared to Al₉FeNi. The phase transformation in Al₉FeNi results in the creation of quasicrystal-like rational approximant lattices that align coherently with Al lattices, resembling an epitaxial-like interfacial approach at the Al-Al₉FeNi boundary. Consequently, the quasicrystal-like phase displays an electron configuration in EELS similar to that of Al₉FeNi.

Notably, although Al₃(Zr/Sc) does not directly contribute to the composition of the rational approximant phase, it acts as an epitaxial catalyst. Overlapping crystal planes are observed between most Al₃(Zr/Sc)-rational approximant boundaries (Fig. 16), and their lattices align coherently with the rational approximant planes. This implies fine Al₃(Zr/Sc) particles are dispersed within the matrix, serving as initiation sites for rational approximant growth. During annealing, Al₃(Zr/Sc) and rational approximants mutually grow from the surface towards areas of lower interfacial energy [36].

4. Discussion

In this study, the structural analysis through diffraction and atomic arrangement imaging of the rational approximant phase has revealed characteristics similar to those reported in quasicrystals (Table 4), yet with notable differences. The distinctions include a smaller b-axis length and a star sublattice composed of three atomic layers instead of two, deviating from reported quasicrystal structures. Furthermore, our experiments demonstrate that this rational approximant phase exhibits a tiling mode where the shield-like tile (SLT) consists of only one type, ensuring the structure's defect-free long-range order and stability. Furthermore, in other similar decagonal rational approximant aluminum alloy systems, the coexistence of quasicrystals and rational approximants is common, where rational approximants are often viewed as an intermediary stage in the transition from quasicrystal to Bravais crystal structures. Literature has reported that some decagonal quasicrystal-like rational approximant systems coexist with quasicrystals. These approximants preserve the symmetry of their parent quasicrystals, indicating a transformational origin [58–60]. An example is Al₆₀Mn₁₁Ni₄, where annealing at 400 °C results in the formation of two rational approximants, orthorhombic and monoclinic [52]. The orthorhombic phase is formed through periodic sub-unit cell twinning, retaining its original diffraction properties. In addition, the Al-Pd-Mn phase from the approximant phase involves a process of segregation and rearrangement of decagonal atom clusters, and these stages can be observed simultaneously [61]. However, in this study, utilizing AM techniques, it has been observed that all Al₆(Cu, Ni)₁(Cr, Mn, Fe)₁

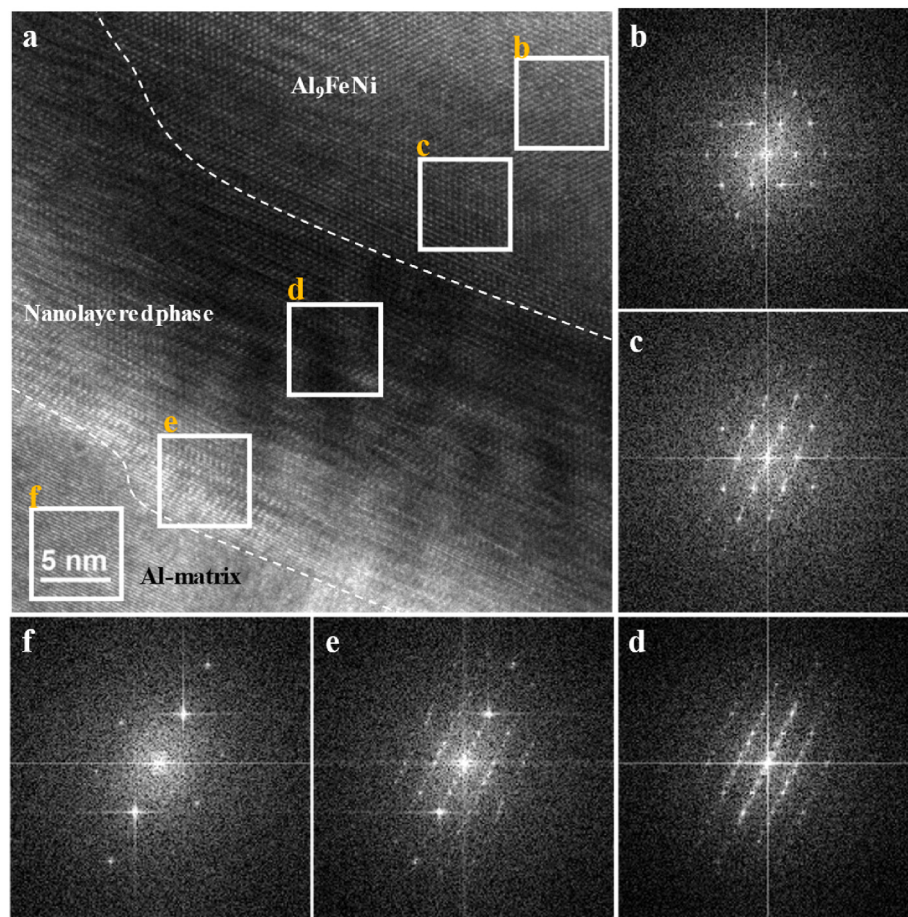


Fig. 15. Continuous Fourier Analysis of Nanolayered Phase. (a) High-resolution TEM image portrays a cross-section through the Al₉FeNi phase, the nanolayered phase, and the Al matrix. (b) The Al₉FeNi lattice, while (c) exhibits the transition region where Al₉FeNi and the nanolayered phase share overlapping diffraction patterns. (d) Highlights the nanolayered phase with its notable tile characteristic. (e) The [111] planes of the α -Al lattice overlap the plane of the nanolayered phase, notably, these planes are parallel to the tile features of the b-axis. (f) Depicts the α -Al FCC structure's diffraction along the [011] zone axis.

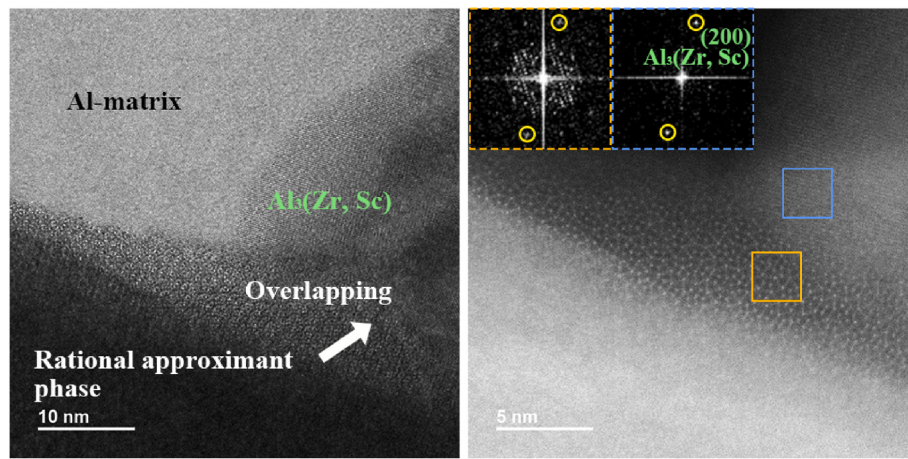


Fig. 16. The relationship of Rational Approximant Phase with Al₃(Zr, Sc) Phase. The atomic-resolution HAADF images capture the quasicrystal and Al₃(Zr, Sc) phase in a state of overlap, illustrating the coherent lattice interconnection. HAADF-FFT patterns demonstrate the overlapping of Al₃(Zr, Sc) (200) planes onto the rational approximant phase.

structures present a uniform rational approximant configuration. This implies that uniform distribution of the rational approximant phase in engineering applications can be ensured through heat treatment at 580 °C for 24 h.

Evidence from this study suggests a link between the formation of the

rational approximant phase and Al₉FeNi, as demonstrated by: (1) The alignment of interplanar d-spacing of [010] with that of Al₉FeNi [100], (2) A gradient of transition elements diffusing from Al₉FeNi along with the observed transition layer, (3) The TEDBs extending from the rational approximant phase to the Al₉FeNi lattice, and (4) The characteristics of

Table 4

Orthorhombic approximate of a rational ratio of two consecutive Fibonacci numbers $\tau = \frac{(1+5^{1/2})}{2}$ ($\cos 36^\circ = \frac{\tau}{2}$). Therefore 1.618 served as golden number in further approximate, l was considered as edge length of the structural blocks. for $a = \frac{l(1+\tau)\sqrt{4-\tau^2}}{\tau}$, and $c = \frac{l(2+\tau+\tau^2)}{\tau}$.

	a (nm)	b (nm)	c (nm)
Quasicrystal Al ₆ (Cu, Ni) ₁ (Cr, Mn, Fe) ₁ (this work)	3.22	0.76	2.37
Al-Cr-Fe-Si (2/3, 1/2) ₂ [16]	3.04	1.23	2.23
C ₃ r-Al ₆₀ Mn ₁₁ Ni ₄ [50]	3.27	1.25	2.38

the nanolayered phase. The lattice of the nanolayered phase can be indexed along the same zone axis as that of adjacent Al₉FeNi. Regarding the cooling rate of AM LPBF technology, the metallurgical mechanisms in this study may differ from traditional processes. Literature indicates that Al₃Ni₂ exhibits structural similarities with decagonal quasicrystals in aluminum alloy decagonal quasicrystal systems [62,63]. Therefore, it can be hypothesized that during the heat treatment following the AM process, the supersaturation and focused diffusion of Cr and Mn at phase boundaries might lead to the evolution of a part of Al₉FeNi into a structure resembling Al₃Ni₂, which may further transform into a rational approximant phase. The nanolayered lattice arrangement found in this study provides evidence for the possibility of such a transformation. The solid dissolution of Cr and Mn into Al₉FeNi during the additive manufacturing process is pivotal for the transformation into rational

approximants, whereas an insufficient cooling rate may lead to the formation of Al₇Cr and Al₆Mn. The high cooling rates intrinsic to additive manufacturing refine the grain size and establish the necessary conditions for building the rational approximant with senary elements in this study. Subsequent annealing treatments (580 °C for 24 h) facilitate phase transformations in rational approximants, including overcoming mismatches at phase boundaries during grain growth and incorporating diffused Cr and Mn. The formation of additional binary and ternary compounds could potentially raise the system's energy. However, further investigation is still needed to fully understand the phase transformation mechanisms and their relation to quasicrystals in this alloy system. Furthermore, the interaction between Al₉FeNi and Al₃(Zr/Sc) plays a crucial role in forming rational approximant phases. Al₃(Zr/Sc), acting as an epitaxy catalyst at the Al-Al₉FeNi interfaces, aids further growth of quasicrystals. This formation mechanism is schematically represented in Fig. 17. The method of additive manufacturing combined with heat treatment is promising for introducing decagonal quasicrystal-like rational approximant systems into bulk materials, leading to the production of stable, defect-free aluminum quasicrystal-like alloy materials. This approach may have significant implications for future engineering applications.

5. Limitation

This study provides insights into the crystallographic structure of complex intermetallic phases, primarily focusing on atomic

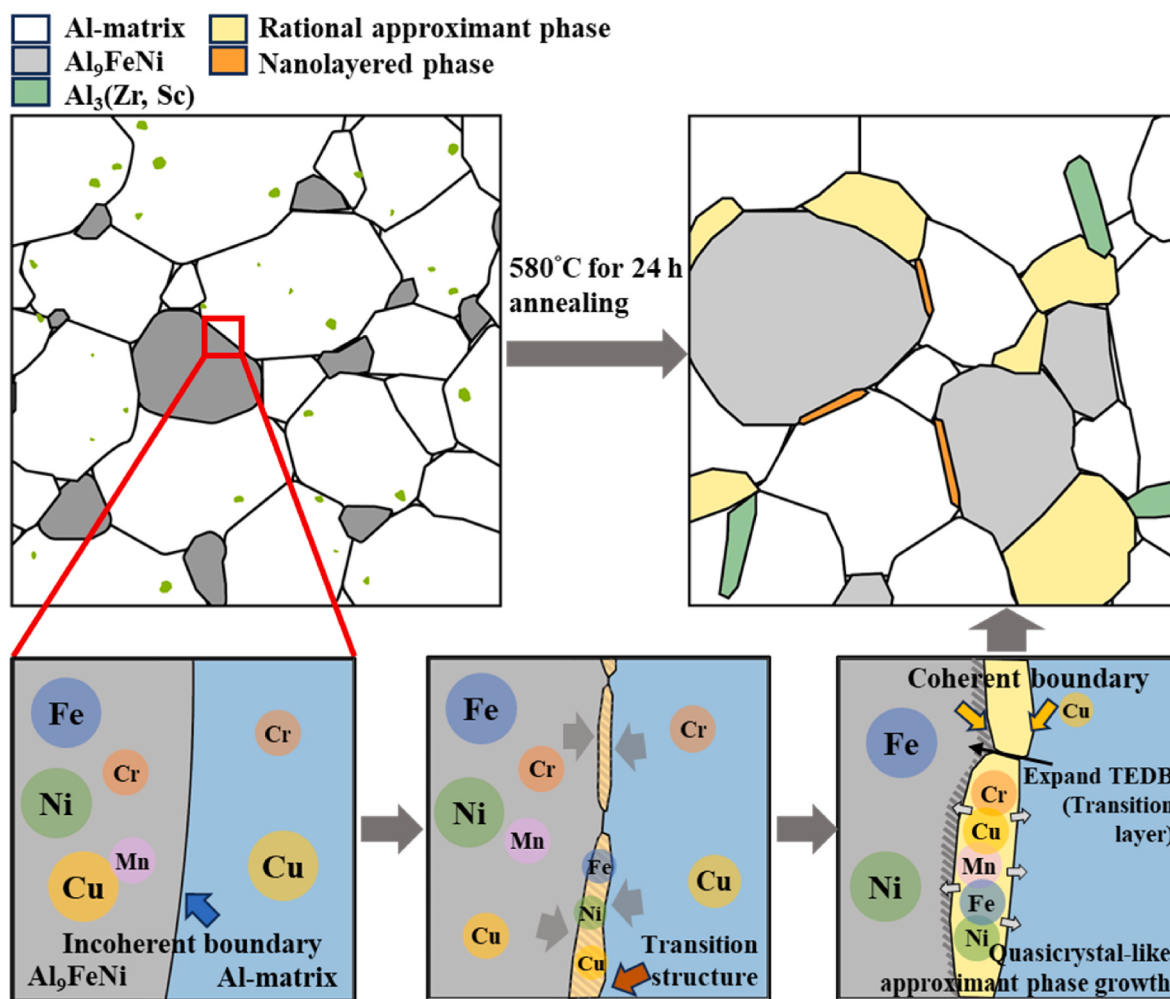


Fig. 17. Evolutionary Mechanism of Rational Approximant Phase Formation. This schematic illustrates the possible transformation mechanism from Al₉FeNi to the rational approximant phase on the incoherent interface.

arrangements. However, practical applications, particularly under high-temperature conditions, remain uncertain due to the limited scope and duration of the research. Consequently, the presumed engineering stability of these phases should be viewed with caution. Rigorous high-temperature testing is essential to validate their performance and ensure the theoretical advancements are applicable and reliable for engineering use.

6. Conclusion

This study showcases the creation of a novel quasi-periodic rational approximant structure, $\text{Al}_6(\text{Cu}, \text{Ni})_1(\text{Cr}, \text{Mn}, \text{Fe})_1$, employing additive manufacturing and long-term annealing. This phase is characterized as a Robinson (R-type) decagonal approximant with both periodic translational and quasi-periodic rotational symmetries. The phase transformation of the rational approximant is driven by the element diffusion of supersaturated solute, forming during the rapid solidification of additive manufacturing. Additionally, overcoming interfacial energy—including grain and phase boundaries—is essential during the prolonged annealing process to promote grain growth. Different from other quasicrystal-like approximant phases, this structure doesn't coexist with quasicrystals and features fewer types of shield-like tiles, presenting a defect-free, three-dimensional tile mode structure.

Additionally, $\text{Al}_3(\text{Zr}/\text{Sc})$ acts as a nucleation site for phase transformation, further simplifying rational approximant formation and contributing to material stabilization. This method addresses the challenges in mass-producing such materials. Additionally, this study also corroborates the viability of using XRD as a preliminary screening tool specially for this system during practical engineering. Considering the unique properties of rational approximants, and combining the advantages of printing Al-Ni-Cu alloy, the capability to control and replicate bulk production holds substantial potential for engineering applications.

CRediT authorship contribution statement

Kai-Chieh Chang: Writing – review & editing, Writing – original draft, Visualization, Methodology, Investigation, Formal analysis, Data curation, Conceptualization. **Fei-Yi Hung:** Writing – review & editing, Supervision, Resources, Project administration, Conceptualization. **Jun-Ren Zhao:** Supervision.

Declaration of competing interest

The authors declare that they have no known competing financial interests or personal relationships that could have appeared to influence the work reported in this paper.

Data availability

No data was used for the research described in the article.

Acknowledgments

The authors thank Taiwan Circle Metal Powder Co., Ltd. and Taiwan ANJI Technology Co., Ltd. for respectively providing the alloy powder and the LPBF printer used in this study. The authors gratefully acknowledge the JEOL JEM-2100F Cs STEM (machine code EM000800), Single-Crystal X-Ray Diffractometer (machine code XRD003100) for technical support, equipment belonging to the Core Facility Center of National Cheng Kung University, Taiwan. The authors thank the National Cheng Kung University Instrument Center and the Ministry of Science and Technology of Taiwan (NSTC 112-2221-E-006-061-MY2) for their financial support.

Appendix A. Supplementary data

Supplementary data to this article can be found online at <https://doi.org/10.1016/j.mtadv.2024.100513>.

References

- [1] D. Shechtman, I. Blech, D. Gratias, J.W. Cahn, Metallic phase with long-range orientational order and no translational symmetry, *Phys. Rev. Lett.* 53 (20) (1984) 1951.
- [2] E.L. Albuquerque, M.G. Cottam, Theory of elementary excitations in quasiperiodic structures, *Phys. Rep.* 376 (4–5) (2003) 225–337.
- [3] R. Penrose, The role of aesthetics in pure and applied mathematical research, *Bull. Inst. Math. Appl.* 10 (1974) 266–271.
- [4] A.E. Madison, Symmetry of icosahedral quasicrystals, *Struct. Chem.* 26 (2015) 923–942.
- [5] C. Janot, J. Pannetier, J.M. Dubois, R. Fruchart, Isomorphism in quasiperiodic structures, *Phys. Lett.* 119 (6) (1986) 309–312.
- [6] K. Saitoh, M. Tanaka, P. Tsai, Structural study of an $\text{Al}_{73}\text{Ni}_{22}\text{Fe}_5$ decagonal quasicrystal by high-angle annular dark-field scanning transmission electron microscopy, *Microscopy* 50 (3) (2001) 197–203.
- [7] W. Steurer, S. Deloudi, Cluster packing from a higher dimensional perspective, in: *Science of Crystal Structures*, Springer, Cham, 2015, pp. 165–170.
- [8] C.S. Lee, G.J. Miller, $\text{Li}_{10}\text{Mg}_6\text{Zn}_3\text{Al}_3$: a new intermetallic phase containing building blocks for decagonal quasicrystals, *Angew. Chem.* 113 (24) (2001) 4876–4878.
- [9] W. Steurer, Gummelt versus Lück decagon covering and beyond. Implications for decagonal quasicrystals, *Acta Crystallogr. A* 77 (1) (2021) 36–41.
- [10] E. Fleury, D.H. Kim, J.H. Lee, S.H. Kim, W.T. Kim, J.S. Kim, Spark plasma sintering of Al-Si-Cu-Fe quasi-crystalline powder, *Metall. Mater. Trans. A* 34 (2003) 841–849.
- [11] P. Gummelt, Penrose tilings as coverings of congruent decagons, *Geometriae Dedicata* 62 (1996) 1–17.
- [12] W. Steurer, Why are quasicrystals quasiperiodic, *Chem. Soc. Rev.* 41 (20) (2012) 6719–6729.
- [13] H. Ma, Z. He, H. Li, T. Zhang, S. Zhang, C. Dong, W. Steurer, Novel kind of decagonal ordering in $\text{Al}_{74}\text{Cr}_{15}\text{Fe}_{11}$, *Nat. Commun.* 11 (1) (2020) 6209.
- [14] H. Li, H. Ma, L. Hou, M. Guo, Z. He, Shield-like tile and its application to the decagonal quasicrystal-related structures in Al-Cr-Fe-Si alloys, *J. Alloys Compd.* 701 (2017) 494–498.
- [15] W. Steurer, T. Haibach, B. Zhang, C. Beeli, H.U. Nissen, The structure of decagonal $\text{Al}_{70} \cdot 5\text{Mn}_{16} \cdot 5\text{Pd}_{13}$, *J. Phys. Condens. Matter* 6 (3) (1994) 613.
- [16] Z. He, H. Li, H. Ma, G. Li, Multiple quasicrystal approximants with the same lattice parameters in Al-Cr-Fe-Si alloys, *Sci. Rep.* 7 (1) (2017) 1–10.
- [17] H. Li, Y. Wang, G. Li, L. You, W. Wang, R. Yu, Z. He, 180° domain related to structurally complex crystals in $\text{Al}_{60}\text{Cr}_{20}\text{Fe}_{10}\text{Si}_{10}$, *Mater. Char.* 158 (2019) 109947.
- [18] W. Steurer, Stable clusters in quasicrystals: fact or fiction, *Philos. Mag. A* 86 (6–8) (2006) 1105–1113.
- [19] J. Nakakura, P. Ziherl, J. Matsuzawa, T. Dotera, Metallic-mean quasicrystals as aperiodic approximants of periodic crystals, *Nat. Commun.* 10 (1) (2019) 4235.
- [20] W. Wolf, B.O. Sitta, L.M. Martini, A.M. Jorge Jr., C. Bolfarini, C.S. Kiminami, W. J. Botta, Effect of Cr addition on the formation of the decagonal quasicrystalline phase of a rapidly solidified Al-Ni-Co alloy, *J. Alloys Compd.* 707 (2017) 41–45.
- [21] K. Stan-Głowińska, Ł. Rogal, A. Góral, A. Wierzbicka-Miernik, J. Wojewoda-Budka, N. Schell, L. Litynska-Dobrynska, Formation of a quasicrystalline phase in Al-Mn base alloys cast at intermediate cooling rates, *J. Mater. Sci.* 52 (13) (2017) 7794–7807.
- [22] S.S. Mishra, T.P. Yadav, N.K. Mukhopadhyay, O.N. Srivastava, Synthesis of fine skeletal structure on Al-Cu-Co decagonal quasicrystals for hydrogen production through steam reforming of methanol, *Int. J. Hydrog. Energy* 45 (46) (2020) 24491–24501.
- [23] Y. Liu, T. Liu, X.Y. Yan, Q.Y. Guo, H. Lei, Z. Huang, R. Zhang, Y. Wang, J. Wang, F. Liu, F.G. Bian, E.W. Meijer, T. Aida, M. Huang, S.Z. Cheng, Expanding quasiperiodicity in soft matter: supramolecular decagonal quasicrystals by binary giant molecule blends, *Proc. Natl. Acad. Sci. U.S.A.* 119 (3) (2022) e2115304119.
- [24] Z. He, H. Ma, H. Li, X. Li, X. Ma, New type of Al-based decagonal quasicrystal in $\text{Al}_{60}\text{Cr}_{20}\text{Fe}_{10}\text{Si}_{10}$ alloy, *Sci. Rep.* 6 (1) (2016) 1–8.
- [25] T. Zhang, L. Zhao, H. Ma, S. Huang, L. You, Y. Zhang, Z. He, The phase transition between decagonal quasicrystal and (1/0, 2/1) approximant in $\text{Al}_{20}\text{Si}_{20}\text{Mn}_{20}\text{Fe}_{20}\text{Ga}_{20}$ high entropy quasicrystal alloy, *J. Alloys Compd.* 910 (2022) 164867.
- [26] Y. Zou, P. Kuczera, A. Sologubenko, T. Sumigawa, T. Kitamura, W. Steurer, R. Spolenak, Superior room-temperature ductility of typically brittle quasicrystals at small sizes, *Nat. Commun.* 7 (1) (2016) 1–7.
- [27] W. Man, M. Megens, P.J. Steinhardt, P.M. Chaikin, Experimental measurement of the photonic properties of icosahedral quasicrystals, *Nature* 436 (7053) (2005) 993–996.
- [28] A. Ramakrishnan, K.K. Kesavan, S. Chavhan, M.R. Nagar, J.H. Jou, S.W. Chen, H. W. Haiao, J.M. Zuo, L.Y. Hung, Liquid exfoliation of decagonal quasicrystals and its light out-coupling performance in organic light-emitting devices, *Adv. photonics Res.* 1 (2) (2020) 2000042.
- [29] T.P. Yadav, N.K. Mukhopadhyay, Quasicrystal: a low-frictional novel material, *Curr. Opin. Chem. Eng.* 19 (2018) 163–169.

- [30] S.K. Verma, A. Bhatnagar, M.A. Shaz, T.P. Yadav, Mechanistic understanding of the superior catalytic effect of $\text{Al}_{65}\text{Cu}_{20}\text{Fe}_{15}$ quasicrystal on de/re-hydrogenation of NaAlH_4 , *Int. J. Hydrogen Energy* 48 (26) (2023) 9762–9775.
- [31] D. Nolan, W. Senaratne, D. Baker, L. Liu, Optical scattering from nanostructured glass surfaces, *Int. J. Appl. Glass Sci.* 6 (4) (2015) 345–355.
- [32] Z. Li, X. Li, X. Lin, H. Wang, Y. Fu, B. Zhang, J. Wu, Z. Xie, Highly efficient organic light-emitting diodes employing the periodic micro-structured ITO substrate fabricated by holographic lithography, *Org. Electron.* 75 (2019) 105438.
- [33] R. Chen, H. Wang, Z. Sun, B. He, Study of icosahedral quasi-crystalline phase $\text{T}_2\text{-Al}_6\text{CuLi}_3$ and transformation in 2A97 Al-Li alloy fabricated by laser additive manufacturing, *Mater. Lett.* 316 (2022) 132014.
- [34] M. Wang, R. Li, T. Yuan, J. Kang, P. Niu, D. Zheng, Z. Fan, The evolution of quasicrystal during additive manufacturing and aging treatment of a Si-modified Al-Mn-Sc alloy, *Mater. Sci. Eng. A* 859 (2022) 144206.
- [35] M. Buttard, B. Chehab, R. Shahani, F. Robaut, G. Renou, C. Tassin, E. Rauch, P. Donnadieu, A. Deschamps, J. Balandin, G. Martin, Multi-scale microstructural investigation of a new Al-Mn-Ni-Cu-Zr aluminum alloy processed by laser powder bed fusion, *Materialia* 18 (2021) 101160.
- [36] M.X. Li, H.R. Leonard, S. Rommel, C. Hung, T.J. Watson, T. Polycandriotes, R. J. Hebert, M. Aindow, Use of laser glazing to evaluate an Al-Cr-Co-Mn-Zr alloy containing icosahedral quasicrystalline dispersoids as a candidate material for additive manufacturing, *Addit. Manuf.* 59 (2022) 103114.
- [37] A.P. de Araujo, C.S. Kimitami, V. Uhlenwinkel, P. Gargarella, High-temperature tensile properties of an aluminum quasicrystal-forming alloy manufactured by laser powder bed fusion, *Mater. Sci. Eng. A* 886 (2023) 145670.
- [38] B. Yavas, C.J. Hung, M. Li, R.J. Hebert, S.P. Alpay, M. Aindow, Laser glazing of a quasicrystal-reinforced Al-Cu-Fe-Cr alloy: implications for use in additive manufacturing, *Scr. Mater.* 226 (2023) 115249.
- [39] N. Kang, Y. Fu, P. Coddet, B. Guelorget, H. Liao, C. Coddet, On the microstructure, hardness, and wear behavior of Al-Fe-Cr quasicrystal reinforced Al matrix composite prepared by selective laser melting, *Mater. Des.* 132 (2017) 105–111.
- [40] K.C. Chang, J.R. Zhao, F.Y. Hung, Effects of hyper-high-temperature solid-solution treatment on microstructure evolution and nanoprecipitation of the Al-Ni-Cu-Fe-Zr-Sc alloy manufactured by selective laser melting, *J. Alloys Compd.* 883 (2021) 160781.
- [41] K.C. Chang, J.R. Zhao, F.Y. Hung, Effects of the microstructure and texture characteristics on mechanical properties of the Al-Ni-Cu-Fe alloy manufactured by laser powder bed fusion, *J. Mater. Res. Technol.* 27 (2023) 3411–3423.
- [42] G. Rödler, F.G. Fischer, J. Preußner, V. Friedmann, C. Fischer, A. Weisheit, J. H. Schleifbaum, Additive manufacturing of high-strength eutectic aluminum-nickel alloys—Processing and mechanical properties, *Jo J Mater Process Technol* 117315 (2021).
- [43] J. Deng, C. Chen, X. Liu, Y. Li, K. Zhou, S. Guo, A high-strength heat-resistant Al–5.7 Ni eutectic alloy with spherical Al_3Ni nano-particles by selective laser melting, *Scr. Mater.* 203 (2021) 114034.
- [44] T. Kimura, T. Nakamoto, T. Ozaki, T. Miki, Microstructures and mechanical properties of aluminum-transition metal binary alloys (Al-Fe, Al-Mn, and Al-Cr) processed by laser powder bed fusion, *J. Alloys Compd.* 872 (2021) 159680.
- [45] W. Steurer, S. Deloudi, Decagonal quasicrystals—What has been achieved, *C R Phys* 15 (1) (2014) 40–47.
- [46] C. Dong, J.M. Dubois, S.S. Kang, M. Audier, The orthorhombic approximant phases of the decagonal phase, *Phil. Mag. B* 65 (1) (1992) 107–126.
- [47] K.C. Chang, J.R. Zhao, F.Y. Hung, Microstructure, mechanical properties, and fatigue fracture characteristics of high-fracture-resistance selective laser melting Al-Ni-Cu alloys, *Metals* 11 (1) (2021) 87.
- [48] A. Kiselev, M. Engel, H.R. Trebin, Confirmation of the random tiling hypothesis for a decagonal quasicrystal, *Phys. Rev. Lett.* 109 (22) (2012) 225502.
- [49] T. Seki, E. Abe, Local cluster symmetry of a highly ordered quasicrystalline $\text{Al}_{58}\text{Cu}_{26}\text{Ir}_{16}$ extracted through multivariate analysis of STEM images, *Microscopy* 64 (5) (2015) 341–349.
- [50] H.X. Sui, K. Sun, K.H. Kuo, A structural model of the orthorhombic C31- $\text{Al}_{60}\text{Mn}_{11}\text{Ni}_4$ approximant, *Philos. Mag. A* 75 (2) (1997) 379–393.
- [51] S. Ranganathan, A. Subramaniam, K. Ramakrishnan, Rational approximant structures to decagonal quasicrystals, *Mat. Sci. Eng. A* 304 (2001) 888–891.
- [52] G. Van Tendeloo, J. Van Landuyt, S. Amelinckx, S. Ranganathan, Quasi-crystals and their crystalline homologues in the $\text{Al}_{60}\text{Mn}_{11}\text{Ni}_4$ ternary alloy, *J. Microsc.* 149 (1) (1988) 1–19.
- [53] Z. He, D. Wei, X. Shen, Y. Chen, H. Ma, L. Wang, K. Du, Y. Yao, R. Yu, Approximants of Al-Cr-Fe-Si decagonal quasicrystals described by single structural block, *J. Alloys Compd.* 647 (2015) 797–801.
- [54] V. Demange, J.S. Wu, V. Brien, F. Machizaud, J.M. Dubois, New approximant phases in Al-Cr-Fe, *Mater. Sci. Eng. A* 294 (2000) 79–81.
- [55] H. Ma, Z. He, L. Hou, W. Steurer, Exceptionally large areas of local tenfold symmetry in decagonal $\text{Al}_{59}\text{Cr}_{21}\text{Fe}_{10}\text{Si}_{10}$, *J. Alloys Compd.* 765 (2018) 753–756.
- [56] P.J. Steinhardt, H.C. Jeong, K. Saitoh, M. Tanaka, E. Abe, A.P. Tsai, Experimental verification of the quasi-unit-cell model of quasicrystal structure, *Nature* 396 (6706) (1998) 55–57.
- [57] Z. He, J.L. Maurice, H. Ma, Y. Wang, H. Li, T. Zhang, X. Ma, W. Steurer, Experimental observation of carousel-like phason flips in the decagonal quasicrystal $\text{Al}_{60}\text{Cr}_{20}\text{Fe}_{10}\text{Si}_{10}$, *Acta Crystallogr. A* 77 (5) (2021).
- [58] S. Ranganathan, K. Chattopadhyay, A. Singh, K.F. Kelton, Decagonal quasicrystals, *Prog. Mater. Sci.* 41 (4) (1997) 195–240.
- [59] A.I. Goldman, R.F. Kelton, Quasicrystals and crystalline approximants, *Rev. Mod. Phys.* 65 (1) (1993) 213.
- [60] S. Ranganathan, A. Subramaniam, Orthorhombic rational approximants for decagonal quasicrystals, *Bull. Mater. Sci.* 26 (2003) 627–631.
- [61] W. Sun, High-resolution electron microscopy study of the early stage of formation of a Al-Pd-Mn decagonal quasicrystal from its crystalline approximant, *Phil. Mag. Lett.* 73 (6) (1996) 395–404.
- [62] X.Z. Li, K.H. Kuo, Decagonal quasicrystals with different periodicities along the tenfold axis in rapidly solidified Al-Ni alloys, *Philos. Mag. Lett.* 58 (3) (1988) 167–171.
- [63] C. Pohla, P.L. Ryder, Crystalline and quasicrystalline phases in rapidly solidified Al-Ni alloys, *Acta Mater.* 45 (5) (1997) 2155–2166.